Collective vortex dynamics and heat transport in a neutron star

Jack Lönnborn

Supervisor: Andrew Melatos

University of Melbourne

A thesis submitted for the degree of

Master of Science (Physics)

November 6, 2018

Acknowledgements

Statement of contribution

- Chapter 1 is a review of the literature relevant to this report, written by me. Section 1.3 was drafted by me with substantial editing by Andrew Melatos.

- Chapter 2 is based closely on the following paper:

  Lönnborn, J. R., Melatos, A. and B. Haskell, *Collective, glitch-like vortex motion in a neutron star with an annular pinning barrier*, Monthly Notices of the Royal Astronomical Society (2018), submitted.

  The paper has been refereed. It received a favourable review with minor emendations requested. The work is my own and the text was drafted by me with substantial editing by Andrew Melatos. The numerical calculations in this chapter were done using a Gross-Pitaevskii equation solver written by Tapio Simula and used with his permission. The glitch detection algorithm was written by me, based on the description in Warszawski & Melatos (2011). The vortex finding algorithm was written by James Douglass. All figures are my own.

- The work in Chapter 3 is my own. The numerical calculations were performed using a code written by me to solve the heat equation in one and two-dimensions.
- The work in Chapters 4 is my own. The numerical calculations were performed using a code written by me to solve the hydrodynamic equations for a neutron superfluid.

Other acknowledgements

I would like to express my gratitude to Andrew Melatos for his enthusiasm for and interest in this project, his encouragement, and for taking the time to share his knowledge with me. I would also like to thank Lisa Drummond, Bryn Haskell, Tapio Simula, Joe Berry and everyone in 359 for their help and support.

Abstract

A neutron star is the dense remnant of a supernova, when a medium-mass star runs out of fuel, collapses, and explodes. The densities in the inner core can reach few $\times\ 10^{15}\,\mathrm{g\,cm^{-3}}$, while the magnetic fields in highly magnetized neutron stars are of order $1 \times 10^{15}\,\mathrm{G}$. Rotating neutron stars, which can have millisecond spin periods, are observed when electromagnetic radiation beamed along their magnetic axis sweeps across the earth in regular pulsations. The extreme densities and low temperatures in mature neutron stars are thought to give rise to superfluid and superconducting phases in the interior.

The superfluid in the core and inner crust mimics the solid-body rotation of the rigid, outer crust by nucleating an array of quantised vortices. Neutron star glitches— sudden, impulsive changes in the spin period— are commonly believed to occur, when angular momentum is transferred suddenly from the star's interior to the crust by the collective unpinning and repinning of large numbers of superfluid vortices. In general, the pinning potential associated with nuclei in the crustal lattice varies as a function of radius. In Chapter 2, we explore vortex dynamics under these conditions by solving the three-dimensional Gross-Pitaevskii equation in a rotating, harmonic trap with an axisymmetric 'moat' of deeper pinning sites on an otherwise uniform, corotating pinning grid. It is shown that vortices accumulate in the moat, inducing large differential rotation which can trigger mass unpinning events. It is also shown that the system self-adjusts, such that the net vortex flux out of the system is the same with and without a moat, as the trap spins down, but the glitches are less frequent and larger when the moat is present.

In binary systems, accretion drives nuclear reactions which deposit heat in the crust. We study diffusive heat transport in an accreting neutron star with radially-dependent thermal conductivity in Chapter 3. Low conductivity in the core is shown to trigger steep temperature gradients which heat successively deeper layers and, in some circumstances, deposit more energy in the core in the steady state than is deposited for higher conductivities. In a superfluid, the temperature fluctuations also obey a wave equation, and propagate convectively. In Chapter 4, we investigate how the onset of superfluidity alters the inward transport of thermal energy. We build a hydrodynamic model and find that diffusion tends to quench the convective modes of the superfluid. It is shown that a mismatch in the thermal conductivities of the crust and core gives rise to large velocities in the proton-electron fluid.

Contents

Chapter 1

Introduction

Neutron stars are compact astronomical objects which are a possible end product of stellar evolution. A compact object is born when a progenitor star has consumed most of its fuel and can no longer generate sufficient thermal pressure to support itself against gravitational collapse. If the progenitor is sufficiently massive ($8 \lesssim M/\mathrm{M}_\odot \lesssim 60$), it will explode in a core-collapse supernova and expel the material of its outer layers (Shapiro & Teukolsky, 2004). The object which is left behind is called a neutron star, and is believed to be supported against further collapse by neutron degeneracy pressure.

Studying the neutron star interior gives unique insight into fundamental physics in extreme conditions. The simultaneous unpinning of trillions of superfluid vortices is thought to cause pulsar glitches, which we introduce in Section 1.3. Understanding the interactions between nuclei and vortices in the crust of neutron stars, and their relation to vortex avalanches and pulsar glitches, is the subject of Chapter 2. In binary systems, accretion triggers nuclear burning on the neutron star surface. How is the thermal pulse transported into the interior, and how does superfluidity in the core alter the diffusive conductivity of degenerate electrons? Thermal transport in accreting binaries is studied in Chapters 3 and 4. In the remainder of this chapter, we introduce the background necessary to explore these problems.

1.1 Neutron star composition

The Fermi energy of an electron gas in three-dimensions is $\epsilon_\mathrm{F} \propto n_\mathrm{e}^{2/3}$, so that ϵ_F is large as we move deeper into the neutron star. Consequently, we have $m_\mathrm{p} + m_\mathrm{e} + \epsilon_\mathrm{F} > m_\mathrm{n}$ (where m_n, m_p and m_e are the neutron, proton and electron masses respectively), and electron capture is energetically favourable:

$$p + e \rightarrow n + \nu. \tag{1.1}$$

The result is that stellar interior is particularly neutron rich, with neutrons in the core alone making up $\gtrsim 90\%$ of the total mass (Link, 2003).

Observational data from thermonuclear X-ray bursts suggest neutron star radii in the range $10 \lesssim R/\mathrm{km} \lesssim 13$ (Coleman Miller & K. Lamb, 2016). The observed mass distribution peaks at approximately $1.28\,\mathrm{M}_\odot$ for neutron star-neutron star binaries, and $1.48\,\mathrm{M}_\odot$, for neutron star-white dwarf systems (Özel et al., 2012). The most massive known neutron star is the recently-observed PSR−J2215+5135 with $M = 2.27^{+0.17}_{-0.15}\,\mathrm{M}_\odot$ (Linares et al., 2018). The internal composition is stratified: a magnetosphere, atmosphere, outer and inner crust, and outer and inner core, with densities ranging from $10^6\,\mathrm{g\,cm^{-3}}$ in the atmosphere to few $\times\, 10^{15}\,\mathrm{g\,cm^{-3}}$ in the inner cores of massive neutron stars (Shapiro & Teukolsky, 2004). The properties of each

layer are as follows.

The atmosphere is thought to be a thin plasma of light elements (Romani, 1987), with a magnetosphere consisting of charged particles corotating with the star (Shapiro & Teukolsky, 2004; Chamel et al., 2013). Although this stratum contains only a very small amount of the star's mass, it has a large effect on the emergent photon spectrum (Lattimer & Prakash, 2004). The outer crust comprises a crystalline solid of heavy, neutron-rich nuclei and a degenerate, relativistic electron gas (Pethick & Ravenhall, 1995). The transition to the inner crust occurs at the neutron drip density $\rho \approx 4 \times 10^{11} \mathrm{g\,cm^{-3}}$. Nuclei at these densities are so neutron rich that the outermost occupied states become unbound, and neutrons 'drip' from nuclei to form a neutron superfluid in the $^1\mathrm{S}_0$ pairing state (Pethick & Ravenhall, 1995; Chamel et al., 2015). The outer core begins about 1 km from the surface and spans a density range $4.3 \times 10^{11} \lesssim \rho/(\mathrm{g\,cm^{-3}}) \lesssim 10^{14}$ (Haensel et al., 2007). Neutrons in the outer core pair in the $^3\mathrm{P}_2$ state and superfluid protons form a type-II superconductor (Baym et al., 1969a; Gezerlis et al., 2014). The inner core begins at a density of $\rho \approx 2\rho_0$ and is present only in massive neutron stars (Shapiro & Teukolsky, 2004). Its composition is unknown. Suggestions include hyperons (Gusakov et al., 2009), condensates of pions and kaons (Haensel et al., 2007), deconfined quark matter (Glendenning, 1992), and color-superconducting phases (Bedaque & Schaefer, 2002; Alford et al., 2008).

1.2 Introduction to superfluidity

Bosons, unlike fermions, have integer spin and do not obey the Pauli exclusion principle. This has the consequence that, when cooled to near absolute-zero, a large number of particles in a gas of weakly interacting bosons accumulate in the ground state (Pethick & Smith, 2008). This state, described by a macroscopic quantum wavefunction Ψ, is known as a Bose-Einstein condensate (BEC) and has several surprising and remarkable properties. These include irrotational flow with zero viscosity, divergent heat capacity, and formation of a quantised array of microscopic vortices. Although ^{4}He atoms are strongly interacting, they undergo a phase transition when cooled below $T_\mathrm{c} = 2.17\,\mathrm{K}$ (at 1 atm) to a superfluid state which shares many of the features of BECs (Pethick & Smith, 2008). Superfluid ^{4}He was first observed by Kapitza (1938) and Allen & Misener (1938), predating laboratory BECs by about six decades. In this section we consider superfluidity in the context of both ^{4}He and cold quantum gases, as well as astrophysical neutron superfluids in neutron stars.

1.2.1 Vortices in rotating superfluids

The wavefunction Ψ which describes the collective behaviour of particles in a BEC is characterised by a fluid density ρ and macroscopic phase S:

$$\Psi(\mathbf{x}, t) = \sqrt{\rho(\mathbf{x}, t)} e^{iS(\mathbf{x},t)}, \tag{1.2}$$

with ρ, $S \in \mathbb{R}$. The current density is given by

$$\begin{aligned} \mathbf{j}(\mathbf{x}, t) &= \frac{i\hbar}{2m}\Big(\Psi^* \nabla\Psi - \Psi \nabla\Psi^*\Big) \\ &= \rho\Big(\frac{\hbar}{m}\nabla S\Big), \end{aligned}$$

and the superfluid velocity is

$$\mathbf{v}(\mathbf{x},t) = i\hbar\Big(\Psi^*\nabla\Psi - \Psi\nabla\Psi^*\Big)/(2m|\Psi|^2) \tag{1.3}$$

$$= \frac{\hbar}{m}\nabla S, \tag{1.4}$$

where $m = 2m_n$ is the mass of a Cooper pair. It follows from Equation (1.4) that the velocity field is irrotational:

$$\nabla \times \mathbf{v} = 0.$$

Since Ψ is single-valued, the change in phase around a closed loop must be an integer multiple of 2π, so that

$$\oint \nabla S \cdot d\mathbf{l} = 2\pi l, \tag{1.5}$$

where l is an integer. Using Equation (1.4), we obtain a quantisation condition for the circulation Γ around a closed contour,

$$\Gamma = \oint \mathbf{v} \cdot d\mathbf{l} = \frac{\hbar}{m} 2\pi l, \tag{1.6}$$

and define the quantum of circulation $\kappa = 2\pi\hbar/m$. Note that the circulation vanishes for any path enclosing a region which is simply connected. If the path encloses a zero of the density field, however, the region is multiply connected and $\Gamma \neq 0$. This is the result that angular momentum in a BEC is supported by defects in the superfluid topology which are called vortices. A multiply-quantised ($l > 1$) vortex in a harmonically confined condensate is energetically unfavourable, so that a rotating BEC supports an array of l singly-quantised vortices (Shin et al., 2004).[1]

Because κ is of order $10^{-7}\,\mathrm{m^2\,s^{-1}}$ for a neutron superfluid, the number of vortices in a rotating neutron star is very large. For solid body rotation, $\mathbf{v} = \boldsymbol{\Omega} \times \mathbf{r}$, where $\boldsymbol{\Omega}$ and $\mathbf{r}$ are the angular velocity and position perpendicular to the axis of rotation respectively, so that the circulation per unit area is 2Ω. Comparing this to Equation (1.6), we find that the vortex number density is

$$n_v = \frac{2\Omega}{\kappa}.$$

For a neutron star rotating at 100 Hz, $n_v \approx 1 \times 10^5\,\mathrm{cm^{-2}}$. We summarise the evidence for superfluidity in neutron stars in Section 1.2.3.

1.2.2 Two-fluid theory and second sound

The two-fluid model developed by Landau (1941) is a hydrodynamic description of superfluid ^{4}He. Landau treats the superfluid phase as a mixture of a viscous normal component (denoted by the subscript n) and an inviscid superfluid component (denoted by s). The total density of the fluid ρ is the sum of the temperature-dependent densities of the components, ρ_n and ρ_s, each having a corresponding velocity field $\mathbf{v}_n$ and $\mathbf{v}_s$. For $T = 0$ we have $\rho_s/\rho = 1$, while above the superfluid transition temperature all of the density is in the normal component and $\rho_s/\rho = 0$.

[1] We exclude specific configurations of pinning forces designed to stabilise multiply-quantised vortices (Baert et al., 1995), and rapidly rotated condensates where metastable 'giant' vortex cores have been observed (Engels et al., 2003).

The atoms in the superfluid component are in the ground state and have zero entropy, so that entropy is carried only by the normal fluid.

The hydrodynamic equations which govern the two-fluid system can be linearised and written in the form of two wave equations (Landau & Lifshitz, 1986):

$$\partial^2\rho/\partial t^2 = \nabla^2 p, \tag{1.7}$$

$$\partial^2 s/\partial t^2 = (\rho_s s^2/\rho_n)\nabla^2 T, \tag{1.8}$$

where p is the pressure, T is the temperature, and s is the entropy per unit mass. Assuming plane wave solutions, we obtain two expressions for the sound speed:

$$u_1^2 = \partial\rho/\partial p, \quad u_2^2 = T s^2 \rho_s/(c_v \rho_n), \tag{1.9}$$

where c_v is the specific heat capacity. The expression for u_1 gives the velocity of ordinary sound waves: perturbations in the density, driven by pressure gradients. u_2 on the other hand corresponds to perturbations in the entropy, driven by temperature gradients. Because entropy is carried only by the normal fluid, this implies local fluctuations in ρ_n. u_2 is only non-zero below T_c and is called the second sound speed.

The usual mechanism for the transport of thermal energy is diffusion. Diffusive heat transfer is introduced in Section 1.4.1 and studied in detail in Chapter 3. The above discussion shows that in a superfluid, the temperature may also propagate as a wave, leading to thermal effects which differ greatly from those occurring in an ordinary fluid. We study the hydrodynamic equations and thermal evolution of a superfluid in a neutron star in Chapter 4.

1.2.3 Evidence for superfluidity in neutron stars

The interior of neutron stars has long been thought to contain a superfluid phase (Migdal, 1959; Ginzburg & Kirzhnits, 1965). The principal motivation for this is the fact that, in all but the youngest neutron stars, the temperature $T \lesssim 0.1\text{MeV}$ is significantly lower than the critical temperature for the onset of $^1\text{S}_0$ neutron pairing at densities typical in neutron star inner crusts, thought to be $T_{\text{cn}} \approx 1\,\text{Mev}$ (Shapiro & Teukolsky, 2004; Gezerlis et al., 2014; Ding et al., 2016; Chamel, 2017). The critical temperature for $^3P_2$ pairing, expected to occur in the core, is less certain, with predictions in the range $0.01 \lesssim T/\text{MeV} \lesssim 0.1$ (Dong et al., 2013; Ding et al., 2016). The strong non-linearity of the pairing interaction complicates calculations of T_{cn}. Regardless of its exact value, cooling simulations suggest that neutron stars typically drop below the critical temperatures for neutron and proton superfluidity within $\approx 10 - 10^2$ years (Chamel, 2017).

Further evidence for superfluidity in neutron stars comes from observations of the neutron star spin period P. The spin period of rapidly rotating neutron stars, known as pulsars, is ordinarily extremely stable, having time variation dP/dt of order 10^{-21} – smaller than the most precise atomic clocks (Hinkley et al., 2013). This is due to the large moment of inertia, which is of order $10^{45}\,\text{g}\,\text{cm}^2$ (Haskell & Melatos, 2015). However, pulsars exhibit sudden, spasmodic spin-up events—known as glitches—in which their rotational frequency Ω jumps by an amount $\Delta\Omega/\Omega \approx 10^{-11} - 10^{-5}$ over less than a day, before relaxing slowly (over days to years) to its extrapolated pre-glitch value (Chamel, 2017; Fuentes et al., 2017). Understanding glitches is a key area of neutron star research, but they are commonly thought to be caused by the dynamics of pinned superfluid vortices (see Haskell & Melatos, 2015, for a review of glitch models). We

explain this mechanism in the next section. A weakly coupled, inviscid superfluid in the interior of the star also explains the long relaxation times observed after some glitches, even if glitches are caused by starquakes or some other mechanism (Baym et al., 1969b).

Recent observations of the surface temperature of the cooling supernova remnant Cassiopeia A provide further support for superfluidity in neutron stars. The rapid decline in temperature—4% over a period of a decade—places strong constraints on possible cooling mechanisms, and is well explained by neutrino emission due to the Cooper pair formation in the core (Page et al., 2011; Shternin et al., 2011). Transiently accreting neutron stars with short thermal relaxation times have also been observed in a number of systems (Shternin et al., 2007; Brown & Cumming, 2009). This is consistent with the presence of superfluid neutrons, whose strongly reduced heat capacity implies much faster thermal equilibration (Chamel, 2017). The thermal evolution of accreting neutron stars is introduced in Section 1.4 and studied in Chapters 3 and 4.

1.3 Vortex pinning and pulsar glitches

1.3.1 Neutron star inner crust

The standard composition of the inner crust of a neutron star is a lattice of nuclei immersed in a sea of superfluid neutrons and degenerate electrons (Baym et al., 1971). As we note in Section 1.2.1, the superfluid nucleates vortices as the star rotates. For the densities found in the inner crust ($4 \times 10^{11} \lesssim \rho/(\mathrm{g\,cm^{-3}}) \lesssim 10^{14}$), first principles calculations suggest vortices pin at or between nuclei in the lattice (Chamel & Haensel, 2008; Avogadro et al., 2008). The nature of this interaction has generally been evaluated by computing the free energies of various static configurations – typically a vortex superposed on a nucleus, and a vortex and a nucleus separated by an infinite distance (Avogadro et al., 2008; Epstein & Baym, 1988; Gandolfi et al., 2015). However, the difficulty inherent to this approach is that it involves subtracting two large energies—of order 10^4 MeV—to compute a quantity which is of order 1 MeV. The high level of accuracy required in this calculation means that even the sign of the interaction (which is a complicated function of the density) is still uncertain (Wlazłowski et al., 2016).

We discuss the details of the microscopic pinning energy further in Section 1.3.2, but the general upshot is as follows. As the star spins down, vortex pinning prevents the superfluid from decelerating with the crust, generating a rotational shear. When the shear reaches a critical value, vortices unpin and transfer their angular momentum to the crust, causing a spasmodic increase in the star's rotational frequency known as a glitch (Anderson & Itoh, 1975). Many (typically $10^7 - 10^{15}$) vortices unpin simultaneously, triggered by various collective knock-on mechanisms (Warszawski et al., 2012). In the absence of pinning, vortex-vortex repulsion (due to the Bernoulli force) is optimized in a triangular Abrikosov lattice (Tkachenko, 1966). The addition of pinning sites distorts this configuration, as vortices self-organize to balance competition between inter-vortex repulsion and attractive or repulsive pinning interactions. The equilibrium is frustrated in general. Frustrated systems have been studied in the context of terrestrial BECs by superposing a corotating square optical lattice on a triangular vortex lattice (Tung et al., 2006). In the astrophysical context it has been shown that frustration due to vortex-flux-tube pinning in a neutron star's outer core leads to superfluid turbulence and microscopic vortex tangles (Drummond & Melatos, 2017, 2018).

Table 1.1: Pinning energy E_p calculated by various authors for different mass densities ρ. Note that E_p is not a monotonic function of density: the end points of the density range do not correspond to the extrema of E_p. Sign convention: $E_p > 0$ for nuclear pinning, $E_p < 0$ for interstitial pinning.

Authors	$\rho\,(10^{13}\,\mathrm{g\,cm^{-3}})$	$E_p\,(\mathrm{MeV})$	Potential
Alpar et al. (1984a)	$[3, 13]$	$[0.5, 3]$	
Epstein & Baym (1988)	$[0.07, 12.6]$	$[-2.5, 15]$	
Donati & Pizzochero (2006)	$[0.15, 13]$	$[-0.81, 3.38]$	
Avogadro et al. (2008)	$[0.17, 6.2]$	$[-6.21, 5.03]$	Skyrme force SLy4
	$[0.17, 6.36]$	$[-18.27, 3.85]$	Skyrme force SkM

1.3.2 Calculations of the pinning energy

The radius and spacing of nuclei in the lattice and the sign of the vortex-lattice interaction depend on density, leading naturally to the suggestion that the strength of pinning varies between different regions of the crust (Negele & Vautherin, 1973; Alpar, 1977; Alpar et al., 1984a; Donati & Pizzochero, 2004, 2006). Until recently, calculations of the vortex-lattice interaction have been semi-classical, based either on Ginzburg-Landau theory (Epstein & Baym, 1988) or the Thomas-Fermi ansatz in the local density approximation (Donati & Pizzochero, 2004, 2006). Lately calculations have also been done using Hartree-Fock-Bogoliubov mean-field theory (Avogadro et al., 2007, 2008), focusing on mesoscopic interactions between a vortex and many pinning sites rather than computing the microscopic force per pinning site (Seveso et al., 2016).

We define the pinning energy E_p as the energy difference between the non-interacting configuration (where the vortex-nucleus separation is large) and the zero-distance configuration (where the vortex core coincides with a nucleus). Positive E_p means that vortex-nucleus pinning is energetically favourable, while negative E_p favors interstitial pinning, which maximizes vortex-nucleus separation. A third possibility occurs when a vortex core is larger than a Wigner-Seitz cell in the nuclear lattice, so that the distinction between nuclear and interstitial pinning breaks down (Donati & Pizzochero, 2006).

Table 1.1 presents values of E_p for different densities calculated by various investigators under conditions relevant to a neutron star. Certain calculations minimize the Ginzburg-Landau free-energy functional (Epstein & Baym, 1988). This approach assumes temperatures close to the superfluid transition ($T \approx 0.5\,\mathrm{MeV}$) and is therefore inapplicable to the inner crust of a mature neutron star with $T \approx 0.01\,\mathrm{MeV}$ (Donati & Pizzochero, 2004). In the latter regime the local density approximation gives reasonable values for quantities integrated over a Wigner-Seitz cell. Realistic density profiles for nuclei are incorporated via Woods-Saxon potentials.

Chamel et al. (2007) compared the Wigner-Seitz approximation to a full band theoretic model of dense neutron star matter. They found that the Wigner-Seitz approximation is accurate at the higher temperatures of young neutron stars and during core-collapse supernovae but it breaks down at lower temperatures ($T \lesssim 0.1\,\mathrm{MeV}$), where entrainment becomes important. These results are extended by calculations of the pinning potential per unit length of the vortex which take into account the rigidity of the vortex and the fact that it interacts with a lattice (Seveso et al., 2016; Wlazłowski et al., 2016). Seveso et al. (2016) found weaker pinning compared to calculations involving a single pinning site but concluded that the largest pinning forces are still sufficient to store enough angular momentum in the crust to explain large glitches, such as those observed in the Vela pulsar. Simulations by Wlazłowski et al. (2016) show that the

pinning force is repulsive (resulting in interstitial pinning), and that its magnitude increases with density in the range $1.4 \times 10^{13} < \rho/(\mathrm{g\,cm^{-3}}) < 3.1 \times 10^{13}$.

The pinning strength is in general a non-monotonic function of density and hence of radius. Alpar et al. (1984a) found (Table 1.1) that E_p grows with increasing density to a maximum of 3 MeV at $\approx 7 \times 10^{13}\,\mathrm{g\,cm^{-3}}$ and falls off at the base of the inner crust. Epstein & Baym (1988) reported a larger E_p range, with the extrema (-8.2 MeV and 15 MeV) both lying towards the middle of the density range, and weaker pinning at the top and bottom of the inner crust. Donati & Pizzochero (2006) found significant nuclear pinning ($2.5 < E_\mathrm{p}/\mathrm{MeV} < 3.5$) only in the layer $2 \times 10^{13} < \rho/(\mathrm{g\,cm^{-3}}) < 5 \times 10^{13}$, with negligible pinning elsewhere. The presence of E_p extrema in the inner crust motivates the study in Chapter 2 of collective vortex motion in the situation where local pinning takes a higher value in an annular 'moat'.

1.4 Accreting neutron stars

The Milky Way contains about 200 known bright X-ray sources, the first of which, Scorpius X-1, was detected in 1962 (Giacconi et al., 1962). It was suggested soon after that the signal from Scorpius X-1 was caused by mass accretion onto a binary neutron star or black hole (Zeldovich & Guseynov, 1966). Strong evidence for this hypothesis came with the discovery that another galactic X-ray source, Centaurus X-3, was pulsing at regular intervals of 4.84 s (Giacconi et al., 1971). The next year Schreier et al. (1972) confirmed that the system was a binary, followed quickly by theoretical work demonstrating that Centaurus X-3 and a third source, Hercules X-1, were in fact accretion-powered pulsars (Tananbaum et al., 1972).

A low-mass X-ray binary (LMXB) is a system in which matter is transfered onto a neutron star or black hole from a low-mass ($M_\mathrm{donor} \leq \mathrm{M}_\odot$) companion star (Liu et al., 2007). Orbital periods in LMXBs are short (typically of the order of minutes or hours), indicating a large loss of angular momentum from the system at some point in the past (Tauris & van den Heuvel, 2006). This is explained by the concept of common envelope evolution, whereby the compact body's orbit takes it through the envelope of its giant companion star, resulting in losses from friction and a shrinking of the orbital radius (Ostriker, 1976). Accretion may be persistent or transient, with mean accretion rates $\langle \dot{M} \rangle$ typically between 10^{-14} and $10^{-9}\,\mathrm{M_\odot\,yr^{-1}}$. A transiently accreting neutron star is expected to be in a quasi-stationary state which is largely insensitive to the precise value of $\langle \dot{M} \rangle$ (Yakovlev et al., 2005).

1.4.1 Crustal heating

There are two heat sources in the outer strata of accreting neutron stars. The first is due to thermonuclear burning of hydrogen in the upper atmosphere (Brown et al., 1998). The energy produced is predominately radiated away, with only a small fraction propagating inwards and heating the core (Fujimoto et al., 1987). The second heat source occurs deep in the crust. During accretion, material in the crust is forced inwards and compacted, driving electron capture. The increasingly neutron-rich nuclei eventually fuse in density-driven pycnonuclear reactions and deposit heat in the crust which diffuses inwards, heating the core and driving it out of thermal equilibrium (Rutledge et al., 2002; Yakovlev et al., 2005). If accretion is sufficiently rapid, neutrino emission is initiated which balances the inward heat flux (Brown et al., 1998).

Table 1.2: Thermal conductivity κ and heat capacity C_p calculated by various authors, for different mass densities ρ and $T = 10^8$ K.

Authors	$\log \rho\,(\mathrm{g\,cm^{-3}})$	$\log \kappa\,(\mathrm{erg\,s^{-1}\,cm^{-1}\,K^{-1}})$
Potekhin et al. (2015)	$[3.8, 10]$	$[14, 16.5]$
Shternin & Yakovlev (2006)	$[9.4, 14]$	$[19.7, 23]$
Gnedin et al. (2001)	$[10, 15]$	$[18, 25.6]$
		$\log C_p\,(\mathrm{erg\,s^{-1}\,cm^{-3}})$
Gnedin et al. (2001)	$[9, 15]$	$[16, 20]$

Brown et al. (1998) have proposed that in the case of transient accretion it may be possible to probe properties of the neutron star crust by observing the cooling light curve—that is, the time evolution of the photon luminosity—after the cessation of accretion as the crust relaxes thermally (see also Ushomirsky & Rutledge, 2001; Colpi et al., 2001; Wijnands et al., 2005). The light curve is sensitive at different times to the conductivity at different depths, so that this technique offers the possibility of probing various density regimes (Horowitz et al., 2015). The material in the crust is completely replaced over the accretion lifetime of an LMXB, so that these properties may differ significantly from those of an isolated neutron star (Brown & Cumming, 2009).

In order to learn about the properties of the stellar interior, observations of the light curve are compared to theoretical models. In general this is done by assuming an equation of state for dense matter and solving the relativistic equations for the thermal evolution of a neutron star interior (Thorne, 1977):

$$\frac{1}{4\pi r^2 e^{2\phi}}\left(1-\frac{2Gm}{c^2 r}\right)^{1/2}\frac{\partial}{\partial r}(e^{2\phi}L_r) = -Q_v - \frac{C_v}{e^{\phi}}\frac{\partial T}{\partial t}, \quad \text{and} \tag{1.10}$$

$$-\kappa\left(1-\frac{2Gm}{c^2 r}\right)^{1/2} e^{-\phi}\frac{\partial}{\partial r}(Te^{\phi}) = \frac{L_r}{4\pi r^2}. \tag{1.11}$$

Here Q_v is the neutrino emissivity, C_v is the specific heat capacity and κ is the thermal conductivity. L_r is non-neutrino, thermal luminosity, and gravitational effects are included by the mass $m(r)$ and metric function $\phi(r)$. In the inner crust the conductivity has radiative and diffusive components, the latter due to electron-electron and electron-ion scattering, and scattering of free neutrons by electrons and ions (neutron-neutron collision rates are small and can be ignored) (Chamel & Haensel, 2008; Potekhin et al., 2015); Table 1.2 summarises values for κ and C_v calculated by various authors for a range of densities and $T = 10^8$ K. These scattering processes imply that κ is a strong function of the impurity parameter,

$$Q_{\mathrm{imp}} \equiv n_{\mathrm{ion}}^{-1}\sum_i n_i(Z_i - \langle Z\rangle)^2,$$

which characterises the distribution of nuclei charge (Itoh & Kohyama, 1994). Calculations by Aguilera et al. (2009) show that conduction by superfluid phonons is important if either the magnetic field strength is large, or temperatures exceed $T \approx 10^8$ K. LMXBs are expected to be weakly magnetised (see Bhattacharya, 1995, for a review), but can achieve $T \approx 8\times 10^8$ K when the accretion rate and Q_{imp} are both large (Brown, 2000).

Equations (1.10) and (1.11) have been studied by many authors (Brown & Bildsten, 1998; Gnedin et al., 2001; Yakovlev et al., 2001; Brown & Cumming, 2009; Viganó et al., 2013;

Lim et al., 2017). If gravitational effects are ignored [$m(r) = \phi(r) = 0$], we recover the one-dimensional heat equation. We study the heat equation for a spherically symmetric neutron star in Chapter 3.

1.4.2 Observations of transient LMXBs

The thermal properties of cooling X-ray transients have been investigated by various authors. Shternin et al. (2007) confirm that the observed light curve of KS $1731-260$ can be explained by a large deposition of heat in the crust during the extended ($\gtrsim 12.5\,\mathrm{yr}$) accretion period. Their model implies a thin, superfluid crust, and rules out the amorphous, low conductivity crust proposed by Brown (2000). These results are confirmed by Brown & Cumming (2009), who constrain $Q_{\mathrm{imp}} < 10$ for the neutron stars KS $1731-260$ and MXB $1659-29$. On the other hand, Horowitz et al. (2015) find that a large Q_{imp} (of order 40) produces late time cooling which agrees with more recent Chandra observations of MXB $1659-29$. Recently Deibel et al. (2016) have found that the late time cooling is consistent with a shell of low-conductivity, amorphous nuclei known as nuclear 'pasta' at the base of the crust.

Brown et al. (2018) use repeated observations of the cooling crust to estimate the energy deposited in the core of MXB $1659-29$ during ≈ 2.5 years of accretion. From this they infer the core temperature and place constraints on neutrino cooling. Observations of cooling transients have also been used to place a lower limit on the heat capacity of the core, ruling out a quark color-flavor-locked phase (Cumming et al., 2017). The very slow cooling of the pulsar IGR J17480 $-$ 2446 is difficult to explain with current models, and may point to continued, low-level accretion or unusual (but currently unknown) crust properties (Degenaar et al., 2013).

1.5 Project synopsis

The remainder of this thesis is structured as follows.

- In Chapter 2, we study vortex pinning and dynamics, and their effect on glitch size and waiting time statistics.
- Diffusive heat transfer in a stratified neutron star is studied in Chapter 3.
- The study of diffusive conductivity in Chapter 3 is extended in Chapter 4, where we build a two-component hydrodynamic model and study the wave-like propagation of temperature in a superfluid.
- In Chapter 5 we briefly summarise our key results and consider future work.

Chapter 2

Collective vortex dynamics

In this chapter we study collective vortex motion and pinning in a neutron star where a ring-like barrier ('moat') of deeper pinning sites at some fixed radius is superposed on a uniform lattice. The aim is to simulate, in an idealized fashion, the density-dependent, stratified pinning in a neutron star proposed by previous authors (see Section 1.3.2 and references therein). The central physical question is: does the moat present a heightened barrier to outward vortex motion, as the star spins down? Or does the vortex array self-adjust to nullify the moat, i.e. do vortices pin preferentially in the moat, increasing the Magnus force locally and thereby lowering the barrier? If self-adjustment occurs, is it complete, or does the moat leave an imprint on vortex motion and glitch statistics?

The chapter is organized as follows. We build an idealized Gross-Pitaevskii model of a decelerating, pinned BEC and study outward vortex drift and vortex avalanche dynamics with and without a moat. In Section 2.1 we describe the Gross-Pitaevskii model. In Section 2.2 we compute the density and velocity fields for representative configurations, with and without a moat, in equilibrium. Section 2.3 compares the outward vortex flux for moats of various depths, as the trap spins down. It is shown that large differential rotation can develop in the vicinity of the moat, and that the vortex array self-adjusts such that the outward vortex flux is approximately unchanged compared to when the moat is absent. In Section 2.4 we present evidence of glitches in the simulations and calculate their size and waiting-time statistics, generalizing previous studies without a moat.

2.1 Gross-Pitaevskii model

Following previous work (Warszawski & Melatos, 2011; Warszawski et al., 2012; Melatos et al., 2015; Drummond & Melatos, 2017, 2018), we study vortex pinning in a neutron star computationally by modelling the system as a weakly interacting BEC in a rotating, decelerating, harmonic trap and solving the time-dependent Gross-Pitaevskii equation (GPE) on a three-dimensional grid (see Simula et al. (2008) and Schneider et al. (2006) for numerical details). There are many reasons why this model is highly idealized. For example, the ratio of pinning sites to vortices in our simulations is of order 10, rather than 10^{10} in a neutron star, the neutron superfluid in a neutron star is not a dilute gas, and so on, as discussed in Haskell & Melatos (2015) and Section 7 in Drummond & Melatos (2018). However, the model is computationally tractable and has a successful record of capturing the collective knock-on processes which cause the scale-invariant behaviour of superfluid vortex avalanches under neutron star conditions (Warszawski & Melatos, 2011; Warszawski et al., 2012; Warszawski & Melatos, 2012, 2013).

In the frame corotating with the trap, at angular velocity Ω, the condensate order parameter

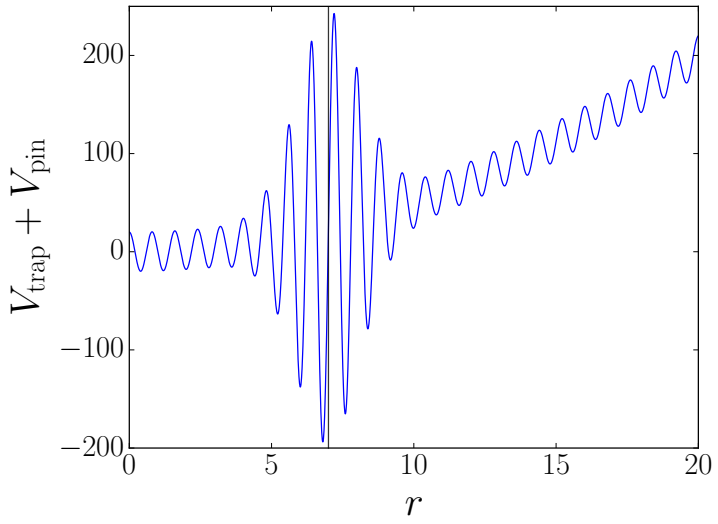

Figure 2.1: Harmonic trap and pinning potential as a function of radius r with $V_{\rm trap} = 0.5(x^2+y^2+\beta z^2)$, $\beta = 32$ ('pancake' geometry), $V_0 = 200$, $V_1 = 20$, $\xi = 1.6$, and $a_0 = 0.4$. The moat is centred on the vertical gray line at $R = 7$.

$\Psi(\mathbf{r}, t)$ is described by the dimensionless stochastic GPE (Gardiner et al., 2002),

$$(i-\gamma)\frac{\partial\Psi}{\partial t} = -\frac{1}{2}\nabla^2\Psi + \big(V + |\Psi|^2\big)\Psi - \Omega\hat{L}_z\Psi + i\gamma\mu\Psi. \tag{2.1}$$

Here μ is the chemical potential, and the term $-\gamma\partial\Psi/\partial t$ ($\gamma \propto T$) models dissipation of sound waves by a viscous thermal cloud; see Warszawski & Melatos (2011) for details. Decreasing γ increases the decay timescale of acoustic pulses emitted by moving vortices, which can unpin further vortices and trigger avalanches (Warszawski et al., 2012). We take $\gamma = 0.1$. Note that Ψ is normalized such that the total number of bosons, N_0, equals $\int d^3\mathbf{r}\,|\Psi(\mathbf{r}, t)|^2$. Length, time and energy in (2.1) are given in units of $\hbar/(m\tilde{n}_0 g)^{1/2}$, $\hbar/(\tilde{n}_0 g)$ and $\tilde{n}_0 g$ respectively, where g is the boson coupling constant and $\tilde{n}_0$ is the mean boson density.

The angular velocity of the trap is updated self-consistently from one time-step to the next according to

$$I_{\rm c}\frac{d\Omega}{dt} = -\frac{d\langle\hat{L}_z\rangle}{dt} + N_{\rm ext}, \tag{2.2}$$

where $I_{\rm c}$ is the moment of inertia of the crust, $N_{\rm ext}$ is the braking torque (of electromagnetic origin in a neutron star), and $\langle\hat{L}_z\rangle = \langle\Psi|\hat{L}_z|\Psi\rangle$ is the expectation value of the angular momentum of the condensate, which responds to changes in vortex positions. We take $N_{\rm ext} = -0.005$ (dimensionless).

In the corotating frame there is a regular periodic lattice of pinning sites representing the crust. The pinning potential $V_{\rm pin}$ increases to a maximum at a fixed radius $r = R$:

$$V_{\rm pin} = \left\{V_1 + V_0 \exp\left[-\frac{1}{\xi^2}\left(\sqrt{x^2+y^2} - R\right)^2\right]\right\}\cos\left(\frac{\pi x}{a_0}\right)\cos\left(\frac{\pi y}{a_0}\right). \tag{2.3}$$

In (2.3), V_0 and V_1 (both positive) are constants setting the strength of the pinning, and a_0 and ξ set the lattice separation and width of the moat respectively. In (2.1), the potential is $V = V_{\rm trap} + V_{\rm pin}$, where $V_{\rm trap}$ is the harmonic trapping potential which confines the condensate, and the depth of the moat is controlled by the ratio V_0/V_1. Figure 2.1 shows a representative example of V versus r; $V_{\rm trap}$ is specified in the caption.

Table 2.1: Number of vortices $N_{\rm vort}$ inside ($|r-R|<\xi$) and outside ($|r-R|>\xi$) moats of different widths. The vortex overdensity (final column) is defined as $[n_{\rm vort}(|r-R|<\xi)-\bar{n}_{\rm vort}]/\bar{n}_{\rm vort}$, where $n_{\rm vort}$ is the local vortex density (number of vortices per unit area) and $\bar{n}_{\rm vort}$ is $n_{\rm vort}$ spatially averaged over the whole condensate. Parameters: $t=1.0$, $V_0/V_1=10$, $a_0=0.4$.

ξ/a_0	$N_{\rm vort}(\lvert r-R\rvert<\xi)$	$N_{\rm vort}(\lvert r-R\rvert>\xi)$	Overdensity
1.58	24	61	2.16
2	16	62	0.85
3	16	63	0.21
4	32	47	0.78

2.2 Representative equilibrium with a moat

2.2.1 Circulation and vortex pattern

We now test how the moat modifies the equilibrium configuration of the vortex array. The system is driven firstly to its ground state by propagating in imaginary time ($t\to it$) with zero spin down. We then propagate the ground-state wavefunction in real time with non-zero spin down, and examine the configuration at a relatively early time, $t=5.0$.

Figure 2.2 plots the condensate density $|\Psi|^2$ without (left panel) and with (right panel) a moat at $R=7$ with $V_0/V_1=10$. Dark blue spots in the condensate are vortices. In the left panel the density decreases away from the axis. In the right panel the condensate 'pools' in the moat: the maximum of $|\Psi|^2$ lies in the region $|r-R|<\xi$. This is a result of the pinning potential; the same effect is present with zero rotation and spin down. Figure 2.3 plots the cumulative number of vortices enclosed within a radius $r=\sqrt{x^2+y^2}$, when there is no moat, and when the moat is centred at $R=7$ and $R=10$. Let the radial distance of the i-th vortex from the origin be denoted by r_i. For $R=7$, we have $2.23\le r_1,\ldots,r_8\le 3.90$, then a plateau in the graph until $6.78\le r_9,\ldots,r_{36}\le 7.69$. Note that $r_{36}-r_9=0.91$ is of order the moat width $\approx\xi=0.63$. The remaining vortices, which have $r_i>R+\xi$, lie in the range $11.90\le r_{37},\ldots,r_{86}\le 14.15$. For $R=10$, we have $2.30\le r_1,\ldots,r_{28}\le 7.59$ and $9.13\le r_{29},\ldots,r_{64}\le 10.93$, so that approximately 42% of vortices are pinned within $|r-R|<2$ of the centre of the moat. The remaining vortices lie in the range $11.90\le r_{65},\ldots,r_{84}\le 13.39$. In both cases, a large number of vortices are pinned in the vicinity of the moat.

Table 2.1 shows the number of vortices pinned in moats of the same depth but different widths. Wider moats do not necessarily pin more vortices than narrower moats of the same depth. However, in all cases the vortex overdensity in the moat, which we define as $[n_{\rm vort}(|r-R|<\xi)-\bar{n}_{\rm vort}]/\bar{n}_{\rm vort}$ where $n_{\rm vort}$ is the local vortex density and $\bar{n}_{\rm vort}$ is the spatially averaged $n_{\rm vort}$, is greater than zero, indicating a greater concentration of vortices in the moat relative to the mean.

The above observations suggest, that the circulation of the fluid (which is proportional to the number of vortices enclosed within radius r) is low for $r<R-\xi$ and high for $r>R+\xi$. We test this by computing the local fluid velocity

$$\mathbf{v}=-i\hbar(\Psi^*\nabla\Psi-\Psi\nabla\Psi^*)/(2m|\Psi|^2). \tag{2.4}$$

Figure 2.4a shows a contour plot of the magnitude of the azimuthal velocity component, $|v_\phi|$. A large number of vortices (identified by red spots, where the fluid velocity is high) are pinned

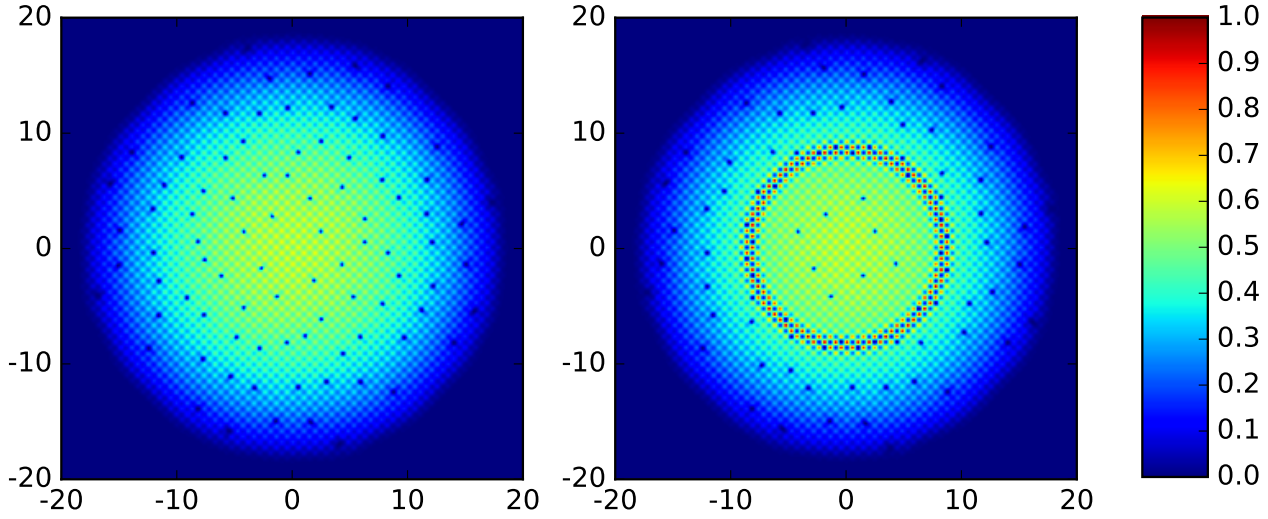

Figure 2.2: Condensate density $|\Psi|^2(x, y)$ (in arbitrary units) without (left panel) and with (right panel) a moat at $t = 5.0$. Blue (red) represents low (high) density. Dark blue spots are vortices. Parameters: same as Figure 2.1.

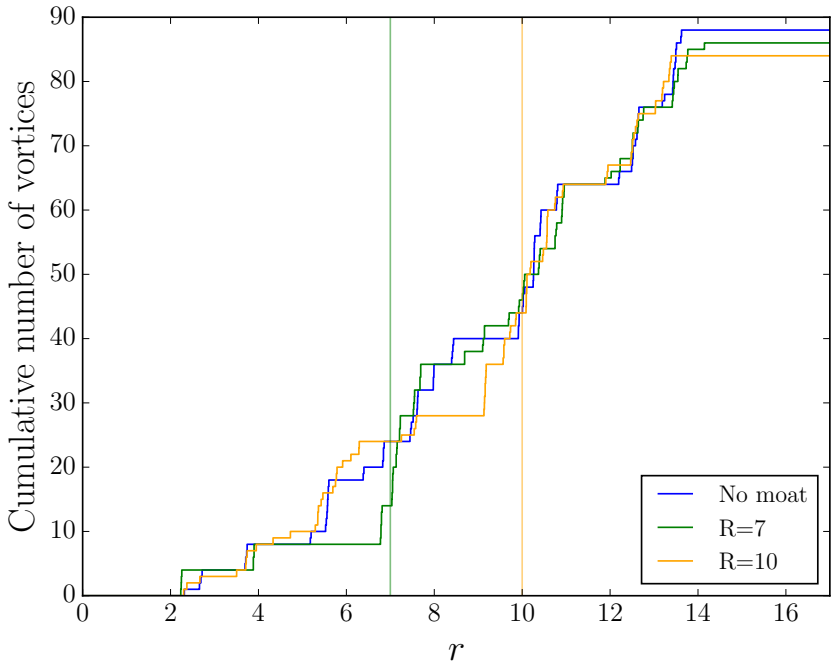

Figure 2.3: The cumulative number of enclosed vortices versus radial distance r from the rotation axis for three different experiments: no moat (blue, $V_0 = 0$), moat at $R = 7$ (green), and moat at $R = 10$ (orange). The centres of the moats are indicated by the vertical green and orange lines. Vortices pin preferentially in the vicinity of a moat. Parameters: $t = 1.0$, $V_0 = 200$, $V_1 = 20$, $\xi = 0.63$, $a_0 = 0.4$.

near the moat at $R = 7$. This causes a large change in the velocity field: the low (blue) values inside the moat increase rapidly for $r \gtrsim R$. The range of velocities represented in the figure is 0 to 2.25% of $|v_\phi|_{\max}$: all pixels with $|v_\phi| \geq 0.0225|v_\phi|_{\max}$ are assigned the same (dark red) color. This is necessary to maintain contrast between pixels which are far from a vortex core because the velocity field diverges inversely with distance from a vortex.

Figure 2.4b plots flow variables of the condensate versus r, averaged over ϕ. The top panel plots the condensate number density $n_0 = |\Psi|^2$, which has a local maximum in the vicinity of the moat, seen also in the right panel of Figure 2.2. The middle and bottom panels show $|v_\phi|$ and the azimuthal current density $|j_\phi| = |\Psi|^2|v_\phi|$ respectively. As $|\Psi|^2$ takes particularly high values in the moat, we plot both $|j_\phi|$ and $|v_\phi|$ in order to verify that the local increase in $|j_\phi|$ near the moat is not just due to $|\Psi|^2$ being higher there. This is important because the Magnus force, which triggers unpinning, is proportional to $|v_\phi|$ not $|j_\phi|$.

Let the relative change in a flow variable X in the vicinity of the moat be defined as

$$\frac{|\Delta X|}{X} = \frac{\max[X(|r-R|<\xi)] - \min[X(|r-R|<\xi)]}{\bar{X}(|r-R|<\xi)}, \tag{2.5}$$

where the overbar indicates a spatial average over values of X in the region $|r-R| < \xi$, and $\min(\cdots)$ $[\max(\cdots)]$ indicates we select the minimum (maximum) value of X in $|r-R| < \xi$. Referring again to Figure 2.4, we find $|\Delta n_0|/n_0 = 0.36$, 0.11 and $|\Delta j_\phi|/j_\phi = 0.75$, 0.11 with and without a moat respectively: larger relative changes occur in n_0 and j_ϕ where there is a moat. Additionally, we find $|\Delta v_\phi|/v_\phi = 0.87$ and 0.20 with and without a moat. Hence the mass current due to the moat is higher not only because $|\Psi|^2$ takes a higher value there; $|v_\phi|$ is also higher.

2.2.2 Moat depth

In this section, we study how varying the depth of the moat, V_0, affects the vortex configuration in equilibrium. Figure 2.5 shows $|v_\phi(r)|$ averaged over circles of constant radius for moats of various depths, with $R = 7$ and $5 \leq V_0/V_1 \leq 10$. The figure shows an increase in $|v_\phi|$ across the moat, with $|\Delta v_\phi|/v_\phi = 1.13$, 1.09, 0.87 for $V_0/V_1 = 5$, 7, 10 respectively, compared to $|\Delta v_\phi|/v_\phi = 0.20$ for $V_0 = 0$. Every simulated moat produces a larger fractional increase in v_ϕ than no moat, but the fractional increase is larger for shallower moats for $5 \leq V_0/V_1 \leq 10$.

An alternative way to quantify the increase in $|v_\phi|$ across the moat is to smooth $|v_\phi|$ with a Savitsky-Golay (low-pass) filter of window size 0.85 and take the gradient of the smoothed function at $r = R$. We find $d|v_\phi|/dr = 0.06$, 0.15, 0.17 for $V_0/V_1 = 5$, 7, 10 respectively, and $d|v_\phi|/dr = -0.003$ for $V_0 = 0$. According to this measure, deeper moats cause a steeper change in v_ϕ. The results for both $|\Delta v_\phi|/v_\phi$ and $d|v_\phi|/dr$ are summarized in Table 2.2. The gradient indicates that the differential rotation and associated Magnus force are high. This is reminiscent of the 'snowplow' model for giant Vela-like pulsar glitches, where a vortex sheet is initially pushed outwards, then released at the maximum of the density-dependent pinning force per unit length (Pizzochero, 2011). In Section 2.4, we explore the dynamical implications by searching for glitches and quantifying their statistics.

The effect of a glitch is to correct accumulated stresses by transferring angular momentum to the crust. Hence a third way to quantify the effect of a moat is to compute the angular

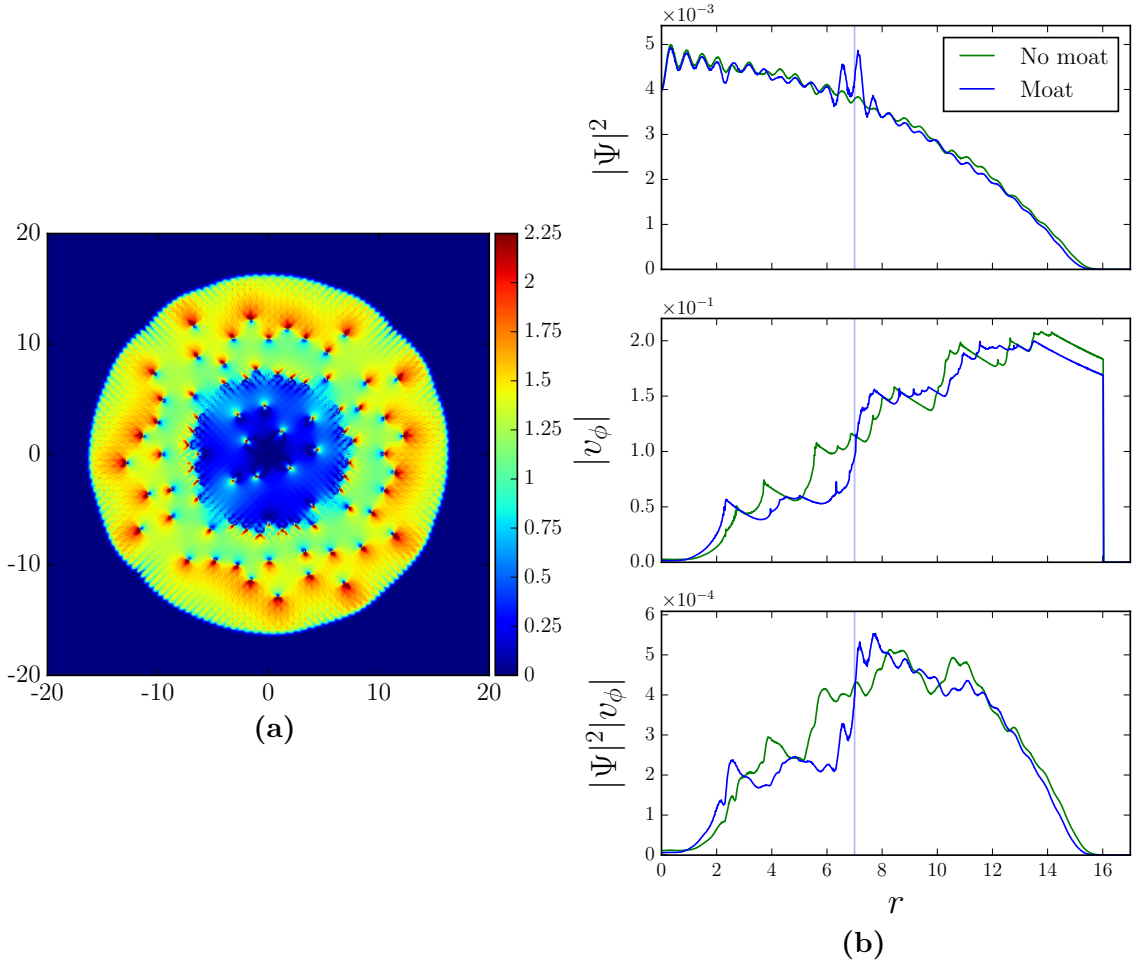

Figure 2.4: Flow variables versus r with and without a moat at $R = 7$. Left panel: Contour plot of the magnitude of the azimuthal condensate velocity $|v_\phi|$ with a moat. The range of values represented in the contour plot is 0 to 2.25% of $|v_\phi|_{\max}$; the numbers on the colorbar indicate a percentage of $|v_\phi|_{\max}$. Right panel, top to bottom: number density $n_0 = |\Psi|^2$, $\hat{\phi}$ component of velocity $|v_\phi|$ and $\hat{\phi}$ component of mass current $|\Psi|^2|v_\phi|$, as functions of radial distance r from the rotation axis and averaged over ϕ with (blue) and without (green) a moat. Parameters: $t = 2.5$, $V_0/V_1 = 10$, $\xi = 0.63$, $a_0 = 0.4$.

Table 2.2: Two measures of the effect of moat depth V_0 on the azimuthal velocity gradient in the moat: $|\Delta v_\phi|/v_\phi$ and $d|v_\phi|/dr$ (dimensionless) (defined in text). Parameters: same as Figure 2.4.

V_0/V_1	$\lvert\Delta v_\phi\rvert/v_\phi$	$d\lvert v_\phi\rvert/dr$
0	0.21	−0.003
5	1.13	0.06
7	1.09	0.15
10	0.87	0.17

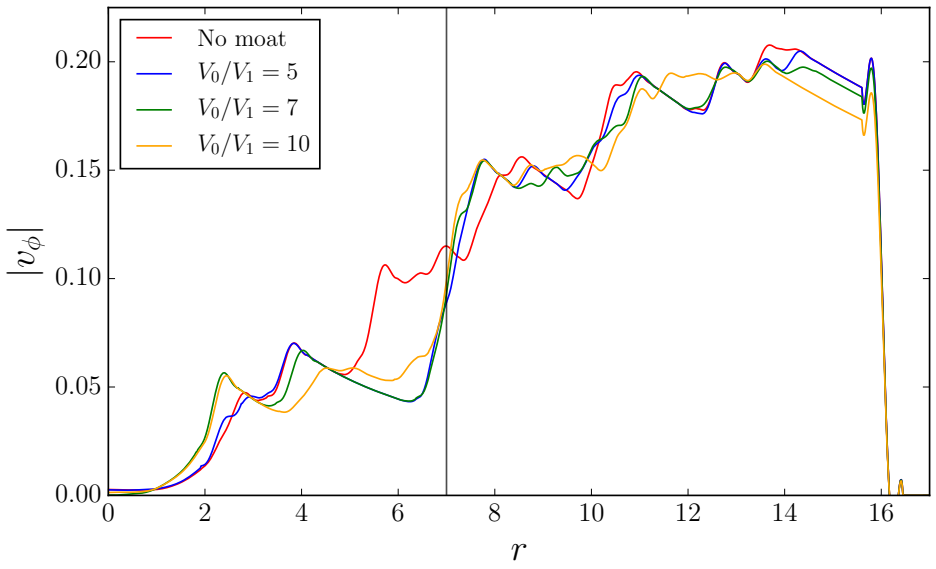

Figure 2.5: The azimuthal component of velocity $|v_\phi|$ (averaged over a circle) versus radius for moats of differing depth with $R = 7$ (vertical gray line). V_0/V_1 quantifies the strength of pinning in the moat relative to the lattice, as defined in Section 2.1. The data has been smoothed with a Savitsky-Golay (low-pass) filter of window size 0.85 to aid readability. Parameters: same as Figure 2.4.

momentum. The total angular momentum of a system of vortices is given by (Fetter, 1965)

$$L = \pi \tilde{n}_0 \hbar \sum_i (Y^2 - r_i^2), \tag{2.6}$$

where Y is the side length of the simulation box in the x and y directions and i labels each vortex. Since the pinning potential affects the spatial distribution of vortices (Figure 2.3, Table 2.1) and hence r_i in (2.6), we expect that a moat should alter the L.

We define the 'excess' contribution to angular momentum from vortices outside the moat as

$$L_{\text{ex}} = L(r_i > R) - L_{\text{NM}}(r_i > R), \tag{2.7}$$

where the subscript NM denotes the no-moat system ($V_0 = 0$), and $r_i > R$ indicates that we include in L only those vortices with $r_i > R$. The results for $R = 5$, 10 and $V_0/V_1 =$ 20, 10, 5, 2.5 are shown in Table 2.3. We expect the numbers in Table 2.3 to decrease down each column (deeper moats build up greater stresses) but remain positive (any moat builds up more stress than no moat). By and large these expectations hold except for two anomalous data points (both in the $R = 5$ column). However, looking at a single time-step is insufficient here for the following reason. Suppose that we calculate L_{ex} at some time $t = t_c$, and that in one simulation with large V_0/V_1 a glitch occurred just prior to t_c, while in another simulation with small V_0/V_1 the most recent glitch was significantly earlier than t_c. A glitch corrects the build-up of L_{ex}. Hence L_{ex} may be larger in the latter simulation despite the shallower moat: we compared the two simulations at different points in their cycle of building up and correcting, via glitches, stress. We study glitches further in Sections 2.3 and 2.4.

Table 2.3: Angular momentum induced by vortices outside the moat: $L_{\rm ex}$ in units of $\pi\tilde{n}_0\hbar$ [defined by Equations (2.6) and (2.7)] for moats of various depths V_0/V_1. Parameters: $t = 1.0$, $\xi = 0.32$, $a_0 = 1$.

V_0/V_1	$L_{\rm ex}(R=5)$	$L_{\rm ex}(R=10)$
20	163.1	326.6
10	177.2	179.3
5	121.6	119.5
5/2	-21.7	4.8

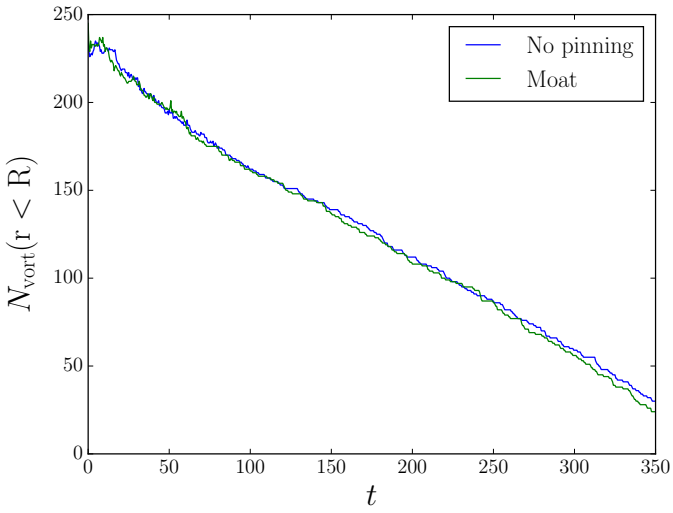

Figure 2.6: Total number of vortices versus time without pinning (blue curve; $V_0 = V_1 = 0$), and with a moat but no lattice (green curve; $V_0 \neq 0$, $V_1 = 0$). Parameters: $V_{\rm pin} = 0$ (blue curve); $V_0 = 200$, $V_1 = 0$, $R = 10$, $\xi = 1.58$, $a_0 = 1$ (green curve).

2.3 Outward vortex flux during spin down

This section looks at the effect of a moat on the spin down of the container. The motivation is partly astrophysical: we wish to know how a shell of stronger pinning affects the long-term deceleration of a neutron star's crust, even though it may be hard to disentangle from other spin-down effects in practice. We find in Section 2.2 that as vortices move radially outwards, they pin in the vicinity of the moat (Figure 2.3). In this respect, the moat acts like a divot or hole on a surface on which a sandpile is forming. Once some critical number of vortices pin near the moat (analogously, once the hole is filled with sand), the question becomes whether the outward vortex flux is the same as without a moat, or whether the flux is altered, retaining an imprint of the moat.

Figure 2.6 graphs the total number of vortices in the system $N_{\rm vort}(r < R)$ as a function of time for no pinning ($V_0 = V_1 = 0$), and for a moat with pinning sites inside it but none outside it ($V_0 \neq 0$, $V_1 = 0$). Anticipating the study of glitch size and waiting time statistics in Section 2.4, we investigate whether the total number of vortices and their distribution in the system, as functions of time, differ between the two cases. For $t \gtrsim 25$ vortices leave the system at an approximately constant rate in both simulations. There is little difference between the two curves: a linear fit to $N_{\rm vort}(r < R)$ versus t gives a gradient of -0.55 without pinning, and -0.57 with a moat, and the maximum difference between the number of vortices in each system is 11 at $t = 16$. If we think of the moat as a defect which perturbs the vortex distribution, then this result suggests that the vortex array self-adjusts to 'heal' the defect: vortices pin near the moat, increasing the local Magnus force and lowering the barrier imposed by the moat so that the outward vortex flux (after some period of equilibration) carries no imprint of the defect.

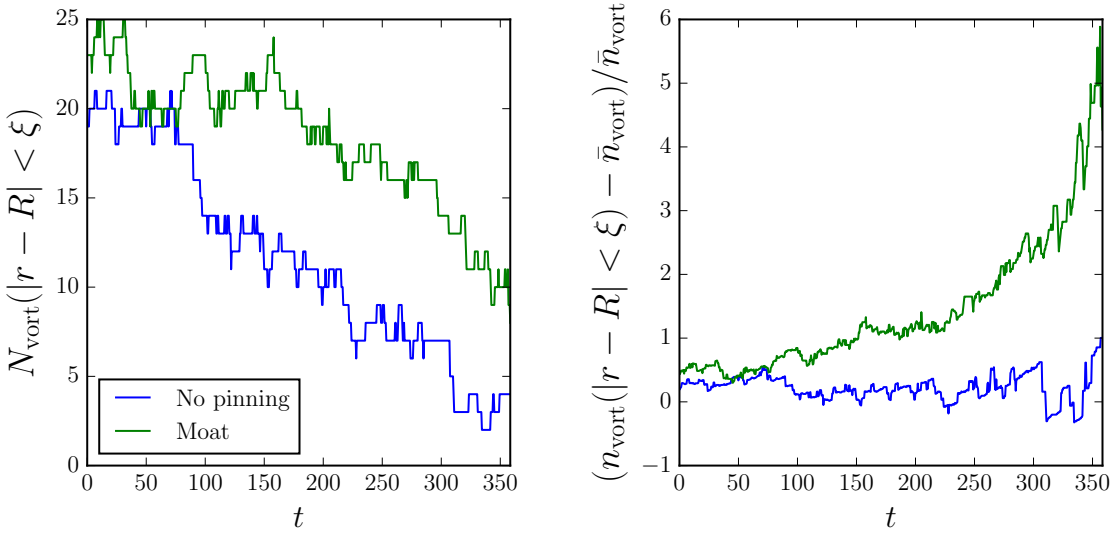

Figure 2.7: The spatial distribution of vortices versus time without pinning (blue curve; $V_0 = V_1 = 0$), and with a moat but no lattice (green curve; $V_0 \neq 0$, $V_1 = 0$). Left panel: number of vortices in the region $|r - R| < \xi$. Right panel: overdensity of vortices in the region $|r - R| < \xi$, $[n_{\rm vort}(|r - R| < \xi) - \bar{n}_{\rm vort}]/\bar{n}_{\rm vort}$, versus time. Parameters: same as figure 2.6.

We now turn to the question of how the vortex pattern evolves in the presence of a moat, given that the net flux of vortices out of the system is unchanged from the no-moat configuration. Figure 2.7 shows the number of vortices pinned in the moat, $N_{\rm vort}(|r-R| < \xi)$ (left panel), and the overdensity of vortices pinned in the moat, $[n_{\rm vort}(|r-R| < \xi) - \bar{n}_{\rm vort}]/\bar{n}_{\rm vort}$ (right panel), as functions of time for the no pinning (blue) and moat (green) configurations. We see that the number of vortices pinned in the region $|r - R| < \xi$ is approximately constant until $t \approx 160$, when it begins to decrease linearly (green curve, left panel). A linear fit to $N_{\rm vort}(|r - R| < \xi)$ versus t for $t > 160$ gives a gradient of -0.05. However the density of vortices pinned in the moat relative to the system as a whole increases with time (green curve, right panel). As the star spins down, both the net flux of vortices out of the moat and the system as a whole is positive, but vortices leave the system as a whole ≈ 10 times faster than they leave the moat. This means that $N_{\rm vort}(|r - R| < \xi)$ and $N_{\rm vort}(r < R)$ both decrease, the latter faster than the former. Figure 2.8 shows a snapshot of $|\Psi|^2$ at two different times, with vortices marked by open green circles. At $t = 250$ (left) the vortex overdensity in the moat is 1.60; by $t = 331.45$ (right) it has risen to 2.94.

2.4 Vortex avalanches

We now study vortex avalanches and spasmodic spin down in order to investigate how a moat affects neutron star spin-down and glitches. In Section 2.4.1 we describe the algorithm used to find glitches in the spin-down data, and in Section 2.4.2 we present glitch size and waiting time statistics.

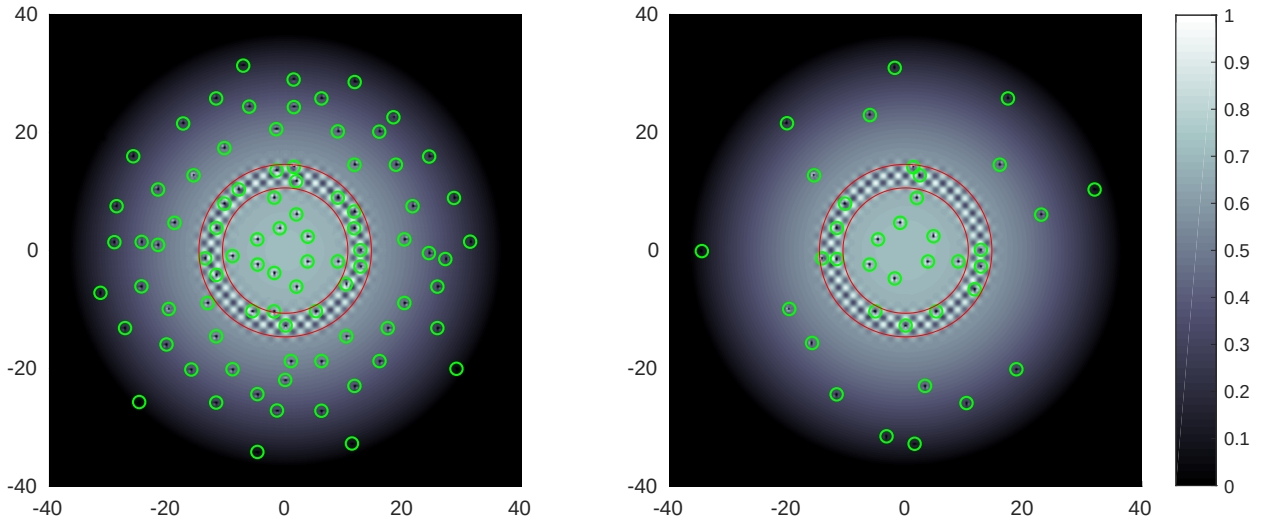

Figure 2.8: Alternative visualization of the vortex overdensity in the moat and its growth with time. Contour plots of the condensate density $|\Psi|^2$ at (left) $t = 250$ and (right) $t = 331.45$. Light (dark) represents high (low) density, vortices are marked by open green circles, and the edges of the moat (at $R \pm \xi$) are indicated by red circles. Parameters: same as figure 2.6.

2.4.1 Glitch detection

In the glitch detection algorithm described by Warszawski & Melatos (2011), $\Omega(t)$ is first smoothed with a top-hat window function of width t_{sm} to combat numerical jitter. A glitch is deemed to occur at time-step i, whenever we have $\Omega(t_{i+1}) > \Omega(t_i)$, that is, whenever the smoothed angular velocity of the condensate increases. Let the end of a glitch t_f be the first time-step after t_i for which $\Omega(t_f) > \Omega(t_{f+1})$, that is, the time-step after which the angular velocity again begins to decrease. We then define the relative glitch size as $\Delta\Omega/\Omega = [\Omega(t_f) - \Omega(t_i)]/\Omega(t_i)$, and the waiting time Δt as the time interval between t_f for successive glitches. Figure 2.9 shows (left panel) the profile of a typical glitch, for different values of the smoothing timescale t_{sm} and (right panel) the number of glitches detected by the algorithm over the whole simulation ($0 \leq t \leq 190.8$) versus t_{sm}. As t_{sm} initially increases from 0, a large number of small glitches are removed, while for $t_{sm} \gtrsim 1.5$ the number of glitches decreases slowly with t_{sm}. We conclude that the true number of glitches is approximately 40, where N_g flattens out, and take $t_{sm} = 0.15$. This coincides with the left panel, where for $t_{sm} > 0.146$ the algorithm detects a single glitch in the time interval $107.6 \leq t \leq 108.8$, as required by eye and the short duration of the timescale over which the multiple peaks in the unsmoothed $\Omega(t)$ occur.

2.4.2 Size and waiting time statistics

The hypothesis that neutron star glitches are produced by avalanche dynamics implies that glitch sizes are distributed as a power law probability density function $[p(\Delta\Omega/\Omega) \propto (\Delta\Omega/\Omega)^{\alpha}]$, and waiting times are distributed as an exponential $[p(\Delta t) = \lambda \exp(-\lambda \Delta t)]$ (Jensen, 1998; Melatos et al., 2008). This motivates the construction of probability density functions of these quantities from the simulations. The left panel of Figure 2.10 shows the size probability density function $p(\Delta\Omega/\Omega)$ on log-log axes with and without a moat (solid green and blue curves respectively). The dashed curves are power-law fits with $\alpha = -0.02$ (moat) and -0.81 (no moat) over

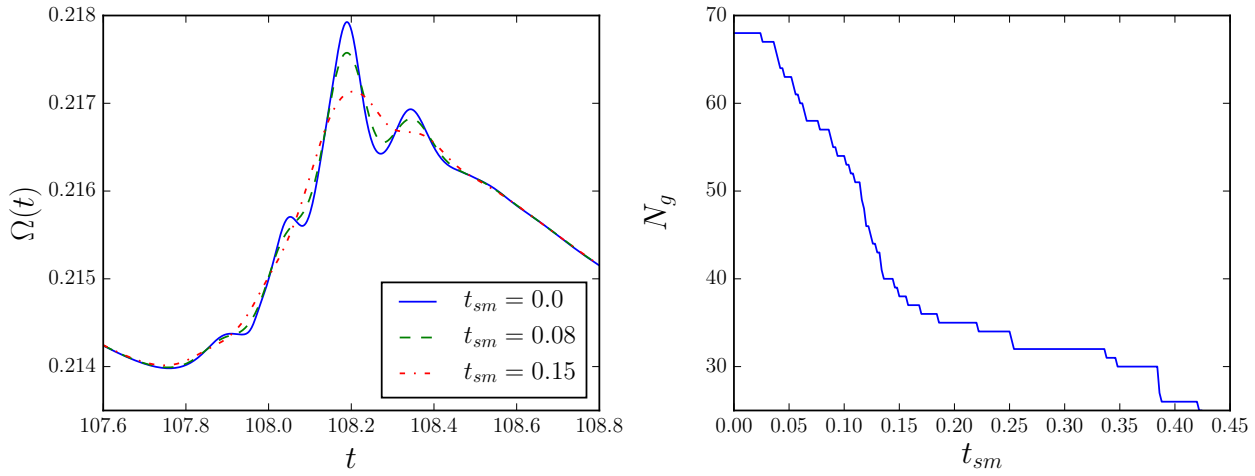

Figure 2.9: Features of the glitch-finding algorithm. Left panel: profile of a typical glitch for different smoothing time-scales t_{sm}. For $t_{sm} > 0.146$ only one glitch is detected in the plotted time interval, $107.6 \leq t \leq 108.8$, as required by eye. Right panel: number of glitches N_g detected by the algorithm over the whole simulation ($0 \leq t \leq 190.8$) versus t_{sm}. The left panel is a reproduction of Figure 5.6 in Warszawski (2011). Both plots are generated from the time series $\Omega(t)$. Parameters: $R = 7$, $V_0/V_1 = 7/3$, $\xi = 1.58$, $a_0 = 1$.

≈ 1.4 decades. We omit glitches with $\log(\Delta\Omega/\Omega) < -3$ as we are interested in the collective vortex dynamics and not small readjustments or 'jiggling' involving few vortices. The right panel of Figure 2.10 shows the waiting time cumulative probability, $P(\Delta t) = \int_0^{\Delta t} d(\Delta t')p(\Delta t')$. An exponential fit to the data gives dimensionless mean glitch rates $\lambda = 0.47$ and 1.44 with ($V_0 \neq 0$) and without ($V_0 = 0$) a moat respectively. The number of glitches detected by the algorithm is $N_g(V_0 \neq 0) = 28$ and $N_g(V_0 = 0) = 204$. There are too few events to properly discriminate between a power law and some other probability density function, and we do not claim that the data demonstrate a power law distribution. Rather, this is a convenient parametrization in keeping with tradition in other work.

For $t_{sm} = 0$ we have $N_g(V_0 \neq 0) = 48$ and $N_g(V_0 = 0) = 592$, $\lambda(V_0 \neq 0) = 1.959$ and $\lambda(V_0 = 0) = 5.674$, and power-law indices $\alpha(V_0 \neq 0) = -0.302$ and $\alpha(V_0 = 0) = -1.098$. As discussed in Section 2.4.1, this case overestimates the true number of glitches by including multipeaked glitches and numerical jitter. For $t_{sm} = 0.3$ we find $N_g(V_0 \neq 0) = 21$ and $N_g(V_0 = 0) = 121$, $\lambda(V_0 \neq 0) = 0.282$ and $\lambda(V_0 = 0) = 0.944$, and $\alpha(V_0 \neq 0) = -0.031$ and $\alpha(V_0 = 0) = -0.476$. Although N_g, α and λ depend on t_{sm}, the overall shape of the probability density functions is similar. Moreover, the ordering of N_g, α and λ is preserved between the moat and no moat cases for a wide range of t_{sm}. Hence we can reasonably comment below on the qualitative effect of a moat on the statistics. We do this in the following paragraph.

The quantitative trends in the glitch statistics are as follows: compared to the no-moat system, a moat gives rise to (i) fewer glitches; (ii) a smaller mean glitch rate λ; and (iii) a smaller power-law index α. That is, a moat gives rise to glitches which are larger but less frequent than those which occur in the absence of a moat. The values of α obtained in the two experiments differ by an order of magnitude, so that we can expect glitches to be significantly larger on average, if a moat is present. The power-law index $\alpha = -0.81$ for an experiment without a moat but with a lattice of pinning sites is comparable to the range $\alpha = -0.994$ to -1.104, for different values of t_{sm}, reported by Warszawski & Melatos (2011). The authors of that paper also report, from exponential fits to $P(\Delta t)$, mean glitch rates of $\lambda = 0.011$ to 0.87 (for different

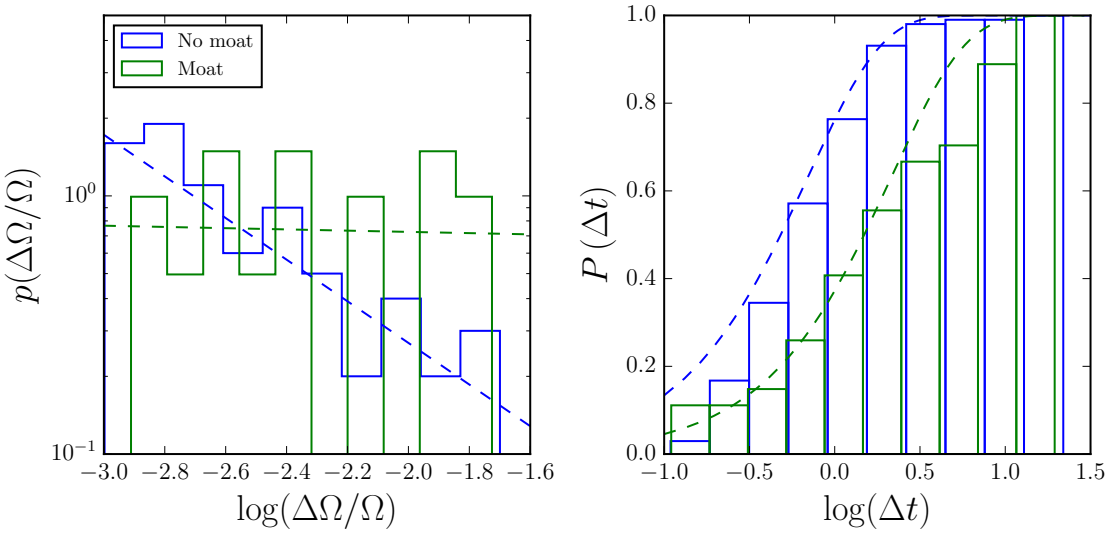

Figure 2.10: Glitch statistics with (green) and without (blue) a moat. Left panel: probability density function (solid curves) of fractional glitch sizes $\Delta\Omega/\Omega$. The dashed curves are power-law fits with $\alpha = -0.81$ (blue) and $\alpha = -0.02$ (green). We omit glitches with $\log(\Delta\Omega/\Omega) < -3$. Right panel: cumulative probability distribution of waiting times Δt. The dashed curves are exponential fits with $\lambda = 0.47$ (green) and $\lambda = 1.44$ (blue). Parameters: $V_0/V_1 = 10/3$, $\xi = 1.58$, $a_0 = 1$, $t_{sm} = 0.15$.

t_{sm}) but find that these fits fail the Kolmogorov-Smirnov confidence test for the null hypothesis that the cumulative waiting time data is drawn from $P(\Delta t)$.

2.5 Conclusions

In this chapter, we study vortex motion in a rotating, decelerating BEC with a uniform grid of pinning sites plus an annular barrier ('moat') of deeper pinning. The ultimate aim is to clarify the role of stratified pinning in a neutron star as input into future, idealized glitch models. We solve the time-dependent GPE and investigate the equilibrium vortex configuration, vortex dynamics and glitch statistics. We find (Section 2.2) that vortices pin preferentially in the moat, so that there is a vortex overdensity in the region $|r - R| < \xi$. The overdensity gives rise to large gradients in the azimuthal condensate velocity at $r \approx R$. The net outward vortex flux is unchanged by the moat, but the vortex flux out of the system as a whole is greater than the flux out of the region $|r - R| < \xi$ (Section 2.3). In other words, the number of vortices pinned in the moat decreases with time, but increases as a fraction of the total number of vortices in the system. The moat produces glitches which are fewer in number but on average larger than without a moat (Section 2.4).

The study in this chapter is motivated by the following specific astrophysical question: is it possible to detect the signature of stratified pinning in a neutron star in its long-term spin-down rate and glitch size and waiting time statistics? Needless to say, the results do not answer this question definitively, because the simulations are idealized in several important ways. For example, the number of vortices in a simulation is of order 100, and the ratio of pinning sites to vortices is of order 10, compared to $10^{16} - 10^{19}$ and 10^{10} in a neutron star, respectively (see Haskell & Melatos (2015)). Nevertheless, two results stand out as likely to be relevant astrophysically: the tendency for vortices to accumulate in moats as the system evolves, and

the reduction in number but increase in size of glitches when a moat is present. Larger GPE simulations containing more vortices and running for longer time intervals will be pursued in future work, although simulations approaching realistic neutron star conditions are beyond the reach of current computer technology.

Chapter 3

Diffusive heat transfer

An accreting neutron star is heated by nuclear burning in the atmosphere, and density-driven, pycnonuclear reactions deep in the crust as neutron rich nuclei are compressed by in-falling matter. These reactions drive the crust and core out of equilibrium, depositing heat which propagates inwards. The crustal lattice can be treated as an elastic solid which at a density of $\rho_c \approx 1.5 \times 10^{14}\,\mathrm{g\,cm^{-3}}$ transitions to the superfluid outer core (Pons et al., 2013). The complex, amorphous arrangements of nucleons thought to occur in the so-called nuclear 'pasta' phase at the base of the inner crust [$8 \times 10^{13}\mathrm{g\,cm^{-3}} < \rho/(\mathrm{g\,cm^{-3}}) < \rho_c$] result in a heterogeneous charge distribution which has been shown to have low electrical and thermal conductivity (Pons et al., 2013; Horowitz et al., 2015). The superfluid core on the other hand is believed to have very high thermal conductivity (Potekhin et al., 2015). More generally, the conductivity is a function of temperature, density, scattering rates and other microphysical inputs, so that we expect it to vary as a function of radius.

In this chapter we study diffusive heat transfer in an accreting neutron star with an initial deposition of thermal energy in the crust. We construct a simple model of the interior with radially-dependent thermal conductivity and solve the heat equation. In Section 3.2 we derive an analytic solution to the one-dimensional heat equation for a stratified, spherically symmetric neutron star. In Section 3.3 we study the steady state solutions and compute the energy deposited in the core. Section 3.4 examines the transient heat flux and thermal relaxation time. The goal in this chapter is not to produce a realistic model for the thermal evolution of a neutron star. For this reason, physical quantities are given in arbitrary units; we indicate realistic values for κ and c_p in Table 1.2. Models with detailed microphysical inputs have been studied by various authors (see Section 1.4). We instead aim to understand how the radial dependence of the conductivity affects diffusive heat transport in general terms. This lays the groundwork for Chapter 4, where we include non-diffusive heat transport associated with a superfluid.

3.1 Heat equation

We can write the equation of conservation of energy in a viscous, thermally conducting fluid with velocity $\mathbf{v}$ in the form (Landau & Lifshitz, 1986)

$$\rho T\left(\frac{\partial s}{\partial t} + \mathbf{v}\cdot\nabla s\right) = \sigma_{ik}\frac{\partial v_i}{\partial x_k} + \nabla\cdot(\kappa\nabla T) + Q, \tag{3.1}$$

where ρ is the density, κ is the thermal conductivity, σ_{ik} is the viscous stress tensor and Q represents sources and sinks. Assuming that the fluid is at rest and using the definition for the specific heat capacity $c_p = T(\partial s/\partial T)$, we obtain the heat equation, which in spherical

symmetry is given by

$$\rho c_p \frac{\partial T(r,t)}{\partial t} = \frac{1}{r^2}\frac{\partial}{\partial r}\left(r^2 \kappa(r) \frac{\partial}{\partial r} T(r,t)\right) + Q(r,t). \tag{3.2}$$

The heat equation is a second order parabolic equation describing diffusion. κ and c_p have units $\mathrm{W}/(\mathrm{m}\cdot\mathrm{K})$ and $\mathrm{J}/(\mathrm{kg}\cdot\mathrm{K})$ respectively, and r is the radial coordinate.

Equation (3.2) can be solved analytically for a composite medium consisting of N layers with left and right boundaries r_i and r_{i+1} respectively, for $i = 1, 2, \ldots, N$ (Vodicka, 1950). Each layer has conductivity κ_i. In composite media, imperfect contact at an interface introduces a heat transfer resistivity. This is a property of the local flow conditions and surface geometry rather than a thermo-mechanical property of the materials, and so is not accounted for by κ. We therefore allow for imperfect heat transfer across an interface by defining the heat transfer coefficient h and dimensionless Nusselt number N (Landau & Lifshitz, 1986):

$$h = \frac{\phi(r,t)}{\Delta T}, \tag{3.3}$$

$$N = hl/\kappa. \tag{3.4}$$

Here $\phi(r,t) = -\kappa \partial T/\partial r$ is the thermal flux per unit area, and l is a characteristic length scale. $\Delta T = T_1 - T_0$ is a characteristic temperature difference across the interface. N and h arise because we are considering a composite medium whose layers are coupled by their shared boundaries (mathematically, by their boundary conditions). Thermal resistance at a boundary usually arises in the context of convective heat transfer, but applies also where the bulk motion of the fluid vanishes as in Equation (3.2) (see section 53, Landau & Lifshitz, 1986, for details).

3.2 Analytic solution

3.2.1 Mathematical formulation

We treat the star as spherically symmetric and composed of $N = 2$ shells—the interior core and exterior crust—and denote the centre of the star, crust-core interface and stellar surface by r_1, r_2 and r_3 respectively. We take ρ and c_p to be uniform throughout the entire star, and the conductivity to be uniform within each region, so that

$$\kappa(r) = \begin{cases} \kappa_1 & \text{if } r < r_2 \\ \kappa_2 & \text{if } r \geq r_2. \end{cases}$$

Given these assumptions, the system of equations is written as

$$\rho c_p \frac{\partial T_i(r,t)}{\partial t} = \frac{\kappa_i}{r^2}\frac{\partial}{\partial r}\left[r^2 \frac{\partial}{\partial r} T_i(r,t)\right] + Q_i(r,t), \quad r_i \leq r \leq r_{i+1}, \tag{3.5}$$

for $i = 1, 2$. For a perfectly insulated boundary at r_i we have zero thermal flux and hence $h = 0$. For zero insulation, the two adjacent regions freely exchange heat so that very close to the interface, the temperature must be the same on either side. Then ΔT vanishes and we

must have $h = \infty$. These considerations motivate the following general conditions on T at the external boundaries:

$$-\kappa_1 \frac{\partial T_1(r_1,t)}{\partial r} = h_1\big[T_1(r_1,t) - y_1(t)\big] \quad \text{and} \tag{3.6}$$

$$-\kappa_2 \frac{\partial T_2(r_3,t)}{\partial r} = h_3\big[T_2(r_3,t) - y_2(t)\big]. \tag{3.7}$$

Here we have specified ambient temperatures $y_1(t)$ and $y_2(t)$ outside the solution domain, at $r = r_1$ and in the stellar atmosphere, $r \geq r_3$. In a neutron star, the crust is blanketed by an insulating iron envelope (Yakovlev et al., 2005), so that $h_3 \approx 0$. Spherical symmetry implies that the flux at the stellar centre must also vanish ($h_1 = 0$). In this case the right hand side of Equations (3.7) and (3.6) vanish and we do not need to specify the ambient temperatures: the central and surface temperatures are outputs of the model. We postpone applying these boundary conditions in order to present a fully general solution with non-zero h_1 and h_3.

At r_2 energy conservation implies continuity of ϕ, so that the boundary conditions take the form

$$\kappa_1 \frac{\partial T_1(r_2,t)}{\partial r} = \kappa_2 \frac{\partial T_2(r_2,t)}{\partial r} \quad \text{and} \tag{3.8}$$

$$-\kappa_1 \frac{\partial T_1(r_2,t)}{\partial r} = h_2\big[T_1(r_2,t) - T_2(r_2,t)\big]. \tag{3.9}$$

Finally, we define an initial temperature distribution in each region, $T_i(r,0)$. Equations (3.5) are two second order partial differential equations. We have specified four boundary conditions and two initial conditions, so the problem is mathematically well posed.

To solve (3.5), we assume solutions of the form

$$T_i(r,t) = U_i(r,t) + \sum_{j=1}^{2} H_{ij}(r) F_j(t) \tag{3.10}$$

with

$$\nabla^2 H_{ij}(r) = 0, \tag{3.11}$$

where $F_1(t) = -y_1(t)$ and $F_2(t) = y_2(t)$. Inserting Equation (3.10) into (3.5) and using (3.11) gives the governing equation for U_i:

$$\rho c_p \frac{\partial U_i(r,t)}{\partial t} + \sum_{j=1}^{2} H_{ij}(r) \frac{dF_j(t)}{dt} = \kappa_i \frac{1}{r^2} \frac{\partial}{\partial r}\left(r^2 \frac{\partial}{\partial r} U_i(r,t)\right) + Q_i(r,t). \tag{3.12}$$

We specify boundary conditions for U_i and H_{ij} such that T_i satisfies the boundary conditions given above. Then H_{ij} is fully determined by a system of linear equations. U_i is found by expansion in a basis which we specify in Section 3.2.3.

3.2.2 Solution of Laplace's equation

Equation (3.11) is satisfied by

$$H_{ij}(r) = A_{ij} r^{-1} + B_{ij}, \tag{3.13}$$

where A_{ij} and B_{ij} are constants. The boundary conditions are

$$\begin{aligned} \kappa_1 \frac{dH_{1j}(r_1)}{dr} - h_1 H_{1j}(r_1) &= \delta_{1j} h_1, \quad -\kappa_1 \frac{dH_{1j}(r_2)}{dr} = h_2 \big[H_{1j}(r_2) - H_{2j}(r_2)\big], \\ \kappa_2 \frac{dH_{2j}(r_3)}{dr} + h_3 H_{2j}(r_3) &= \delta_{2j} h_3, \qquad \kappa_1 \frac{dH_{1j}(r_2)}{dr} = \kappa_2 \frac{dH_{2j}(r_2)}{dr}. \end{aligned} \tag{3.14}$$

H_{ij} is found by writing (3.14) as a system of linear equations and solving for the coefficients A_{ij} and B_{ij}.

3.2.3 Time-dependent solution

We obtain the initial condition for U_i by inserting $T_i(r,0)$ into Equation (3.10):

$$U_i(r,0) = T_i(r,0) - \sum_{j=1}^{2} H_{ij}(r) F_j(0). \tag{3.15}$$

The boundary conditions are

$$\begin{aligned} \kappa_1 \frac{\partial U_1(r_1,t)}{\partial r} - h_1 U_1(r_1,t) &= 0, \quad -\kappa_1 \frac{\partial U_1(r_2,t)}{\partial r} = h_2 \big[U_1(r_2,t) - U_2(r_2,t)\big], \\ \kappa_2 \frac{\partial U_2(r_3,t)}{\partial r} + h_3 U_2(r_3,t) &= 0, \qquad \kappa_1 \frac{\partial U_1(r_2,t)}{dr} = \kappa_2 \frac{\partial U_2(r_2,t)}{dr}. \end{aligned} \tag{3.16}$$

To find U_i, we expand in the series

$$U_i(r,t) = \sum_{m=1}^{\infty} u_m(t) X_{im}(r) \tag{3.17}$$

and apply the operator ∇^2. This yields an eigenvalue problem for each m which has the solution

$$X_{im}(r) = C_{im} M_{im}(r) + D_{im} N_{im}(r), \quad \text{where} \tag{3.18}$$

$$M_{im}(r) = \frac{1}{r} \sin\Big[\Big(\frac{\rho c_p}{\kappa_i}\Big)^{1/2} \gamma_m r\Big], \quad N_{im}(r) = \frac{1}{r} \cos\Big[\Big(\frac{\rho c_p}{\kappa_i}\Big)^{1/2} \gamma_m r\Big], \tag{3.19}$$

C_{im} and D_{im} are constants, and γ_m are the eigenvalues. The eigenfunctions X_{im} obey the same boundary conditions as U_i.

To find C_{im} and D_{im} we again write the boundary conditions as a linear system $\mathbf{Zc} = \mathbf{0}$. $\mathbf{c} = [C_{1m}, D_{1m}, C_{2m}, D_{2m}]^T$ is the vector of coefficients and the matrix $\mathbf{Z}$ encodes the boundary conditions. The eigenfunctions are the roots of the transcendental equation $\det(\mathbf{Z}) = 0$ and satisfy $0 < \gamma_1 < \ldots < \gamma_m < \ldots$.

To obtain the expansion coefficients of U_i we substitute (3.10) and (3.17) into (3.5). This gives a differential equation which has the solution

$$u_m(t) = u_m(0) e^{-\gamma_m^2 t} + \sum_{j=1}^{2} \int_{-\infty}^{\infty} d\tau \Big\{ \Big[h_{mj} \frac{dy_j(\tau)}{d\tau} + q_m(\tau) \Big] e^{-\gamma_m^2 (t-\tau)} \Big\}, \tag{3.20}$$

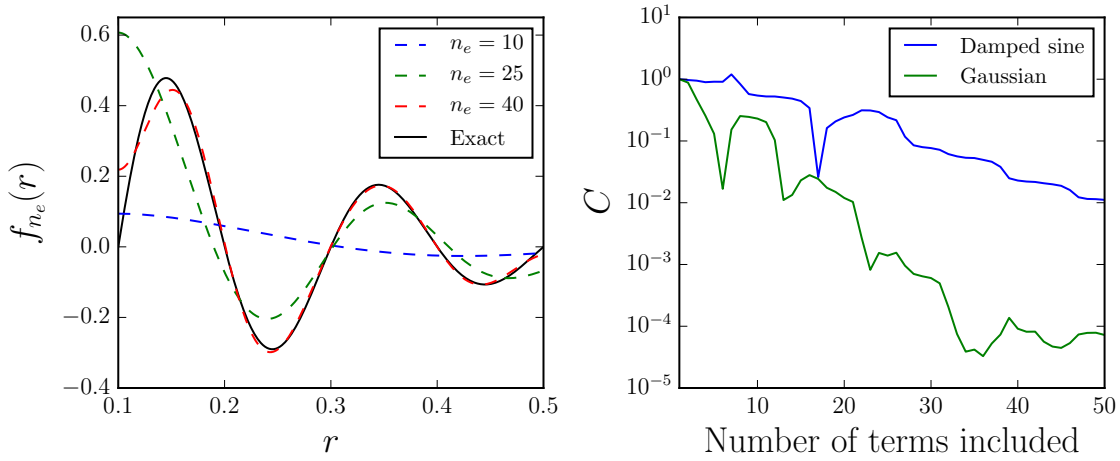

Figure 3.1: Convergence properties of the basis $\{X_{im}\}$. Left: reconstruction of a damped sine wave $f(r) = e^{-5r}\sin[16\pi(r - r_1)/10]$ (solid black line) by the first n_e terms of the series expansion (dashed coloured lines). Right: convergence metric for the series expansion applied to the damped sine wave (blue line) and to a Gaussian, $f(r) = \exp[-(r - 0.3)^2/0.01]$ (green line). The metric C is specified by Equation (3.22).

where Q_i and H_{ij} have been expanded in the basis of eigenfunctions. The expansion coefficients of $Q_i(r, t)$ follow from orthogonality of the basis and are given by

$$q_m(t) = \sum_{i=1}^{2} \left\{ \Big[\int_{r_i}^{r_{i+1}} dr\, r^2 X_{im}(r)^2 \Big]^{-1} \int_{r_i}^{r_{i+1}} dr\, r^2 Q_i(r,t) X_{im}(r) \right\}. \tag{3.21}$$

Replacing Q_i with H_{ij} gives the coefficients h_m. Equations (3.20) and (3.21) and the equivalent equation for h_m determine U_i and complete the formal solution.

Figure 3.1 shows the reconstruction of a test function $f(r) = e^{-5r}\sin[16\pi(r - r_1)/10]$ as the number of terms included in its series expansion is increased (left panel). The right panel shows a metric for how quickly two test functions converge to their exact form as more terms are included in the expansion. The metric is

$$C = \mathrm{abs}\Big[\Big(\int_{r_1}^{r_2} f dr \Big)^{-1} \int_{r_1}^{r_2} (f_{n_e} - f) dr \Big], \tag{3.22}$$

where f is the analytic test function and f_{n_e} is the approximation of f given by the first n_e terms of its expansion. C gives a dimensionless measure for how closely f_{n_e} reproduces f.

3.3 Steady state solutions

We now suppose that there are no sources or sinks ($Q_i(r, t) = 0$ identically), and that the ambient temperatures y_1 and y_2 are constant in time. Then Equation (3.20) implies that the time dependent component of T_i decays exponentially on a timescale dominated by the smallest eigenvalue, so that after some time $T_i(r, t) \approx T_i(r) = \sum_{j=1}^{2} H_{ij}(r) F_i$. In this section we study how these solutions depend on the parameters κ_i and h_2.

3.3.1 Energy deposition in the core

In an accreting neutron star, a fraction f of the energy released from nuclear reactions (outbursts) in the crust propagates into the core, while the remainder $(1-f)$ propagates outwards to the atmosphere and radiates away. Equilibrium is reached when the inflowing heat is balanced by the neutrino flux out of the core, resulting in an inverted temperature profile with a maximum in the stellar crust or ocean. The fraction f and the temperature of the core can be estimated by observing the luminosity after accretion-triggered outbursts (Brown et al., 1998). Estimates of the core temperature from the quiescent luminosity motivate the following astrophysical question: how do the thermal properties of the core and crust affect the amount of energy, in equilibrium, which is deposited in the core? We consider the total thermal energy of the core:

$$U_{\rm core} = \int_{r_1}^{r_2} dr \big[T(r)\rho(r)c_p(r,T)\big]. \tag{3.23}$$

Since we take ρ and c_p to be uniform in $r_1 \leq r \leq r_2$, $U_{\rm core}$ is equal to the integral over $T(r)$, times $m_{\rm core}c_p$, where $m_{\rm core}$ is the core mass.[1] Figure 3.2 plots $U_{\rm core}$ versus κ_1/κ_2 for various h_2 (left panel). Interestingly, $U_{\rm core}$ decreases monotonically with κ_1/κ_2, though the decrease is smallest when h_2 is large. In other words—and somewhat counter intuitively—*more energy is deposited in cores with lower conductivity than in those with higher conductivity.* For $h_2 = 10^5$, $U_{\rm core} = 66.0$ and 51.1 for $\kappa_1/\kappa_2 = 10^{-4}$ and 10 respectively. For $h_2 = 10^{-2}$ the difference is much larger: $U_{\rm core} = 65.6$ and 20.5 for the same κ_1/κ_2.

The h_i chosen here may not reflect actual conditions in a neutron star. As we note in Section 3.2.1, no-flux at the stellar surface and centre implies $h_1 = h_3 = 0$. However, the model neglects sources and sinks of thermal energy due to radiation, viscous flow in boundary layers, and other processes not captured by Equation (3.2). One way to account for these is to relax the no-flux boundary conditions. Similarly, Potekhin et al. (2015) have discussed the idea of a 'bottleneck' at the interface between strata in a neutron star. Within the present framework, this could be incorporated by a finite h_2 which reduces the flux across the crust-core interface. The limiting case of large h_2 is also shown in Figure 3.2. A detailed analysis which accounts for these features in a realistic fashion is beyond the scope of this work. The present result should be understood in this context. It shows that in certain situations (which may not be astrophysically relevant), $U_{\rm core}$ increases with decreasing conductivity.

To explain this physically, we plot (Figure 3.2, right panel) the temperature profiles for different values of κ_1/κ_2 and a representative choice of h_2. In the case of large κ_1/κ_2, the entire star is roughly isothermal in equilibrium. For small values of κ_1/κ_2, on the other hand the crust and outer regions of the core remain hot, while deeper regions are comparatively cool. The trade-off is such that more thermal energy is stored in the core in the latter case than in the former. We conclude by noting that the neutrino luminosity is a function of the mass of the neutron star: high mass neutron stars cool more rapidly (Yakovlev et al., 2005). Hence $m_{\rm core}$ affects $U_{\rm core}$ not only directly through Equation (3.23), but also by setting the equilibrium (in which the diffusive and neutrino fluxes balance) ultimately reached by the system.

[1] The onset of superfluidity, which we do not consider here, has a particularly large effect on this assumption, since the heat capacity of superfluid neutrons is strongly reduced. See Yakovlev et al. (2001), Section 5.5, for details.

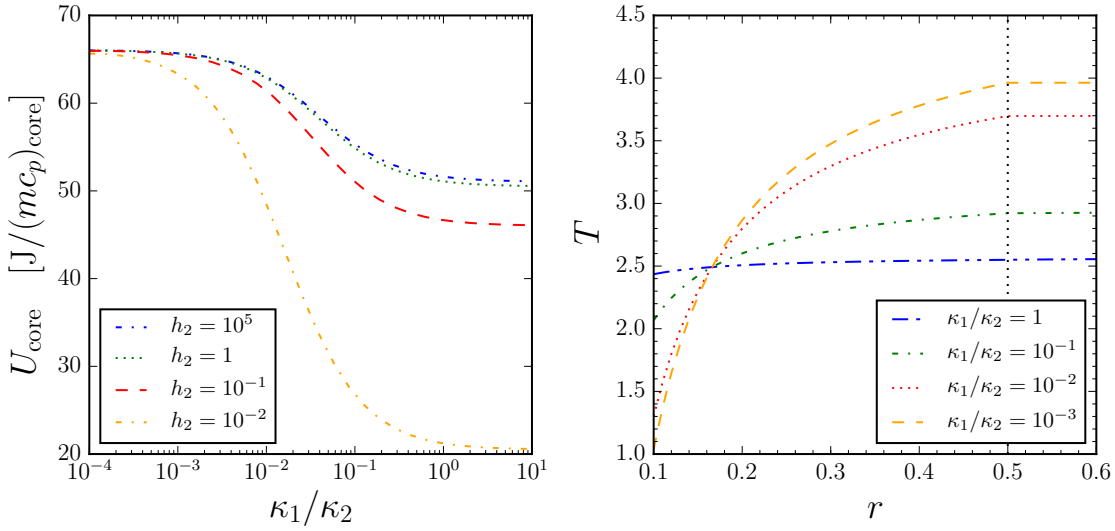

Figure 3.2: Steady state properties of the core. The crust-core interface is at the vertical dotted black line. Left: thermal energy deposited in the core as a function of κ_1/κ_2. Right: temperature profiles for different κ_1/κ_2. Parameters: $h_1 = h_3 = 0.01$, $y_1 = 1$, $y_2 = 4$.

3.4 Transient heat transfer

We now turn to the time-dependent evolution of the system, which for convenience we supplement with a fully numeric code. The code was written by me using the implicit Crank-Nicholson algorithm. In the analytic solution (Section 3.2), the piecewise definition of κ results in a mathematical discontinuity in T. Discontinuous T implies an infinite temperature gradient, which would induce an infinitely large thermal flux. But an infinite flux would instantaneously remove the temperature difference. We conclude that in a physical system T must be everywhere continuous, and ensure this by replacing the piecewise definition for κ with a Fermi function

$$\kappa(r) = (\kappa_1 - \kappa_2)\left[1 + \exp\left(\frac{r - r_2}{\eta}\right)\right]^{-1} + \kappa_2, \tag{3.24}$$

which satisfies $\kappa(r) \approx \kappa_1$ for $r < r_2$ and $\kappa(r) \approx \kappa_2$ for $r > r_2$ for η sufficiently small. We model a thermal pulse on the surface as a narrow Gaussian centred on r_3, which we take as the initial condition for T.

In this section we consider the thermal relaxation of an accreting neutron star, and demonstrate the existence of large thermal gradients and fluxes for certain choices of $\kappa(r)$. Large thermal gradients may be important for several reasons. Andersson et al. (2013) have emphasized that the superfluid transition is a local phenomenon which is triggered by the position-dependent temperature and density. Regions close to the superfluid transition temperature may have a disproportionately large effect on the dynamics. Bildsten (1998) has argued that thermal gradients can trigger asymmetric electron-capture. This causes density asymmetries and hence a mass quadrupole which sources gravitational wave emission and explains the narrow range of frequencies at which rapidly accreting LMXBs are observed to be rotating. These problems depend on the local thermal evolution, which we study below. We do not include nuclear processes or the effects of superfluidity directly, but seek to clarify how temperature gradients depend on the basic thermal properties of the crust and core.

3.4.1 Heat flux

The conductivity in a neutron star is a complicated function of the temperature and microphysics (see Potekhin et al., 2015, for a detailed study). Here we study the general question of how the transient temperature profile depends on κ. Figure 3.3 shows T versus r at equal time intervals for two values of κ_1/κ_2, from $t = 0.02$ (solid blue line) to $t = 0.1$ (solid red line). Low conductivity in the core causes steep temperature gradients ('fronts') to form in the vicinity of the interface and propagate inwards. Figure 3.4 compares the flux at the interface as a function of time for different values of κ_1/κ_2 (left panel). For large κ_1/κ_2, the flux at $r = r_2$ is larger and peaks earlier, but is sustained for a shorter period, than for small κ_1/κ_2. In the latter case, successively deeper layers are heated as the front moves inwards. The right panel shows the flux versus time at different radii for $\kappa_1/\kappa_2 = 10^4$. We see that the flux deep in the core ($r = 0.2$, purple curve) peaks before the flux at $r = 0.65$ (blue curve), so that the interior is rapidly heated.

Figure 3.5 (left panel) plots the radial location of the maximum flux against t for different κ_1/κ_2. For small κ_1/κ_2, the front propagates more slowly inwards, as expected from the above discussion. To study the trade-off between rapid and slow but sustained heating, we integrate $\phi(r = r_2, t)$ for $0 \leq t \leq 0.1$ to find the total energy per unit area which diffuses into the core over that time period, for different κ_1/κ_2 (Figure 3.5, middle panel). For a slowly propagating front corresponding to small κ_1/κ_2, energy is transported more slowly over the interface, resulting in these systems taking longer to relax thermally. This is shown in the right panel, which plots the equilibration time. We consider the equilibration time further in the next section.

3.4.2 Equilibration time

Consider a temperature perturbation δT in a uniform slab of width l. A simple estimate from the heat equation shows that the perturbation relaxes on a timescale given by

$$\tau = \frac{\delta T}{\delta \dot{T}} = \frac{\rho c_p}{\kappa} l^2. \tag{3.25}$$

How quickly does the perturbation relax in a stratified neutron star? This question is relevant to observations of cooling light curves, discussed in Sections 1.4. Slower propagation of the fronts considered in the last section is due to lower conductivity in the core, and corresponds to longer equilibration times.

More precisely, as we note in Section 3.3, τ is dominated by the contribution of the smallest eigenvalue of the time-dependent component, γ_1. Figure 3.5 plots the equilibration time from numerical simulations against κ_1/κ_2 on log-log axes, with $\kappa_2 = 1$ fixed (right panel, blue squares). We say that the system has equilibrated when the temperature at every spatial node in the computational domain is within 0.01% of its final value. The dashed lines are power-law [$\tau = (\kappa_1/\kappa_2)^\alpha$] fits to the data. The sensitivity of the (logarithmic) equilibration time to the core conductivity changes at $\kappa_1/\kappa_2 = 1$, above which it decreases significantly less per increment in κ_1/κ_2. We find $\alpha = -0.82$ for $-6 \leq \log(\kappa_1/\kappa_2) \leq 0$, and $\alpha = -0.12$ for $0 \leq \log(\kappa_1/\kappa_2) \leq 4$.

One immediate question is the following: if we instead fix $\kappa_1 = 1$ and vary κ_2, will the plot of the equilibration time versus κ_1/κ_2 change? In other words, for a given value of κ_1/κ_2, is the equilibration time dependent on whether the region of lower conductivity is in the crust or the core? For brevity we avoid writing out the equation which determines τ [namely $\det(\mathbf{Z}) =$

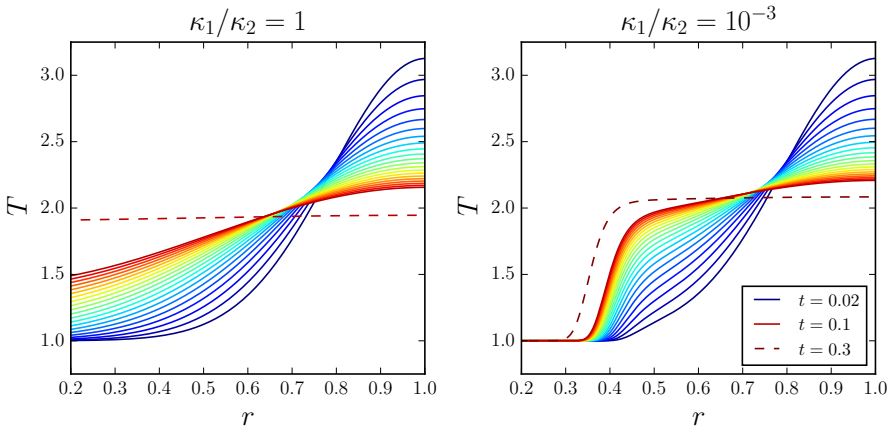

Figure 3.3: Time evolution of temperature T versus r for different κ_1/κ_2. The solid lines are at equally spaced time intervals from $t = 0.02$ (dark blue) to $t = 0.1$ (red); the dashed line is at $t = 0.3$.

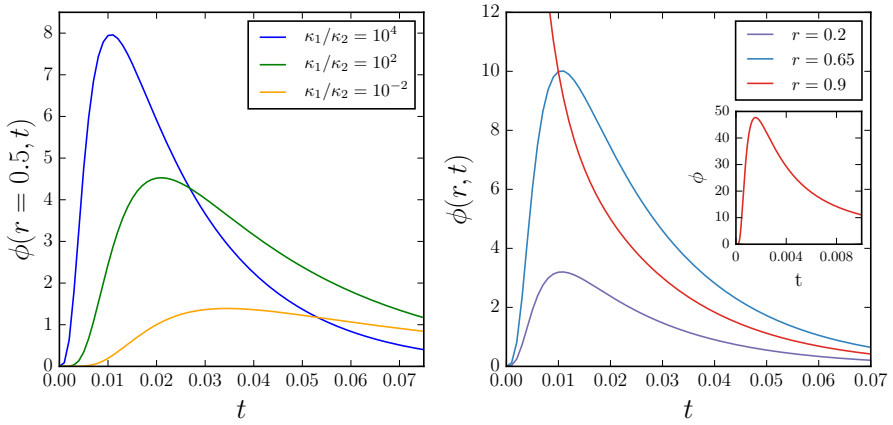

Figure 3.4: Time evolution of the thermal flux ϕ. Left panel: ϕ versus t at the crust-core interface ($r = 0.5$), for different κ_1/κ_2. Right panel: ϕ vs t at different radii, with $\kappa_1/\kappa_2 = 10^4$.

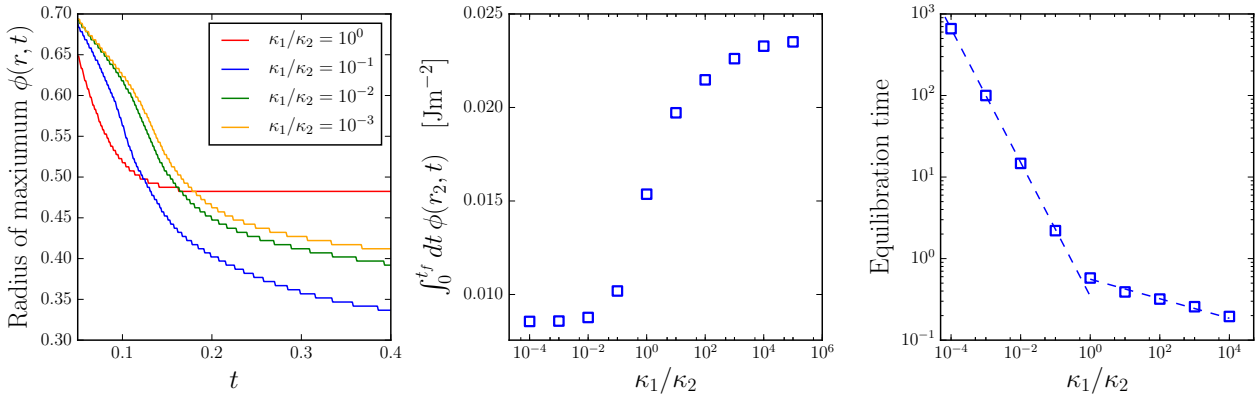

Figure 3.5: Evolution towards equilibrium. Left: Radial location of the maximum thermal flux versus t, for various κ_1/κ_2. Middle: energy per unit area transported over the interface between $t_i = 0$ and $t_f = 0.1$ versus κ_1/κ_2. t_f is chosen to be smaller than the shortest equilibration time for the conductivity ratios plotted. Right: equilibration time versus κ_1/κ_2. The dashed lines are power-law fits to the data in the range $-6 \leq \log(\kappa_1/\kappa_2) \leq 0$ and $0 \leq \log(\kappa_1/\kappa_2) \leq 4$, with indices $\alpha = -0.82$ and $\alpha = -0.12$ respectively. $\kappa_2 = 1$ in the middle and right panels.

0]. However, it is simple to show that viewed as a function of κ_1 and κ_2, $\det(\mathbf{Z})(\kappa_1, \kappa_2) = \det(\mathbf{Z})(\kappa_2, \kappa_1)$, that is, the function is identical under interchange of the two conductivities. The question posed above is therefore answered in the negative: the equilibration time is the same, regardless of whether the crust or core has lower conductivity.

3.5 Conclusions

In this chapter we study diffusive heating in a neutron star with radially-dependent κ. The aim is to understand, in general terms, the thermal evolution following an initial pulse of heat, deposited in the crust during accretion. We derive (Section 3.2) an analytic solution to the heat equation in a stratified neutron star, and study its steady state solutions (Section 3.3). We find that for certain boundary conditions the energy deposited in the core in the steady state is larger for smaller κ_1/κ_2. In Section 3.4 we confirm that large values of κ_1/κ_2 correspond to rapid heating of the core and fast equilibration. On the other hand where κ_1/κ_2 is small, thermal 'fronts'—regions where the temperature gradient is particularly steep—develop at the crust core interface and propagate slowly inwards, heating successively deeper layers. The work in this chapter is extended in Chapter 4, where we solve the hydrodynamic equations for a neutron superfluid, with a diffusive term in the energy equation.

Chapter 4

Superfluid heat transfer

Models of neutron stars at finite temperature typically account for superfluidity by including an additional term in the conductivity and evolving the diffusion equations (1.10) and (1.11). The electron-electron conductivity is believed to dominate (Chamel & Haensel, 2008). As discussed in Section 1.2.2, however, the hydrodynamic equations for laboratory superfluids admit wave solutions not only for the density perturbations, but also for the entropy. Analogous oscillatory modes in the neutron star case have been studied by various authors (Epstein, 1988; Lindblom & Mendell, 1994; Comer et al., 1999; Andersson & Comer, 2001), and recent work suggests that superfluidity in the core of a neutron star can trigger temperature-dependent, convectively-unstable oscillations (Gusakov & Kantor, 2013; Kantor & Gusakov, 2014; Gualtieri et al., 2014; Passamonti et al., 2015). These results challenge the conventional view that thermal effects are weakly affected by the onset of superfluidity.

In this chapter we extend the work of Chapter 3 by solving the hydrodynamic equations for a neutron superfluid and proton-electron component at finite temperature. As in the previous chapter, we study a stratified neutron star with an initial pulse of heat near the surface. The central focus now, however, is to investigate how the heat transport is affected by superfluidity. In other words, we ask how the non-diffusive, convective modes associated with superfluidity alter the diffusive conduction studied in the previous chapter and assumed by many authors.

The chapter is structured as follows. In Section 4.1 we describe the hydrodynamic model. In Sections 4.2 and 4.3 we discuss the numerical implementation of the system of equations, and detail some difficulties encountered in the course of this work. In Sections 4.4 and 4.5 we study convective heating and the response of the proton-electron fluid to the conductivity mismatch. The preliminary calculations presented in these sections were done with a numerical code written by me to solve the equations of motion for the two-component model. We find that convective heating is important at lower conductivities, and that the proton-electron fluid develops a layer where the flow speed is high when there is a large conductivity mismatch between the neutron star strata. We show that the coupling between fluid components affects the size of these velocities, and reduces convective heating in general.

4.1 Hydrodynamics of finite temperature superfluids

4.1.1 Two-component model

A finite-temperature, superfluid description of a neutron star has at least four independent fluid components: neutrons, protons, electrons, and the entropy, which is treated in this framework

as a separate, massless flow (Andersson & Comer, 2006; Lopez-Monsalvo & Andersson, 2011).[1] In this section we make some simple assumptions which reduce the four dynamical degrees of freedom associated with these components to two.

Following previous studies, we assume that the electron fluid is coupled electromagnetically to the proton fluid, so that the net charge current vanishes and there are no global electromagnetic fields (Alpar et al., 1984b; Passamonti et al., 2015). We therefore treat the protons and electrons as comprising a single fluid which we denote by the subscript p. This corresponds to what is called the normal fluid in Landau's model of superfluid ^{4}He, where it refers to the excited modes of a single particle species (see Section 1.2.2). In keeping with this simple picture, however, we assume that the entropy is carried by the proton-electron fluid only. In reality, protons in the core are superconducting, so that only the electrons carry entropy. We do not consider superconductivity in this work (cf. Drummond & Melatos, 2017, 2018).

Although we ignore global electromagnetic fields, we account for coupling between the two fluids due to mutual friction. Mutual friction is a dissipative force which arises due to electron scattering off vortex cores, which carry a magnetic flux due to Fermi liquid interactions. Finally, we note that the two fluids are also coupled via the strong nuclear interaction. This is incorporated via the equation of state, which we present in Section 4.1.3.

4.1.2 Governing equations

The two fluids satisfy the mass conservation equations

$$\frac{\partial \rho_n}{\partial t} + \nabla \cdot (\rho_n \mathbf{v}_n) = 0 \quad \text{and} \tag{4.1}$$

$$\frac{\partial \rho_p}{\partial t} + \nabla \cdot (\rho_p \mathbf{v}_p) = 0, \tag{4.2}$$

and the momentum equations

$$\frac{\partial \mathbf{v}_n}{\partial t} + \mathbf{v}_n \cdot \nabla \mathbf{v}_n = -\nabla \tilde{\mu}_n - \mathbf{F} \quad \text{and} \tag{4.3}$$

$$\frac{\partial \mathbf{v}_p}{\partial t} + \mathbf{v}_p \cdot \nabla \mathbf{v}_p = -\nabla \tilde{\mu}_p - \frac{s}{\rho_p} \nabla T + \mathbf{F}. \tag{4.4}$$

Here $\tilde{\mu}_{\mathrm{x}}$ is chemical potential per unit mass of species x, and s is the entropy per unit volume. $\mathbf{F} = K(\mathbf{v}_n - \mathbf{v}_p)$ is the acceleration due to mutual friction (or any other linear coupling), whose size is controlled by the parameter K (Hall & Vinen, 1956). The entropy transport obeys

$$\frac{\partial s}{\partial t} + \nabla \cdot (s \mathbf{v}_p) = \frac{1}{T} \nabla \cdot (\kappa \nabla T), \tag{4.5}$$

where we include a diffusive term on the right hand side (see, e.g., Chandler & Baym, 1986). Equations (4.1)-(4.5) are nine partial differential equations for the nine dependent variables ρ_n, ρ_p, $\mathbf{v}_n$, $\mathbf{v}_p$ and s.

[1] We do not consider muons, which are present in the core. Their velocity field is coupled to that of the electron fluid by scattering on a timescale $\tau \approx (\hbar/k_B T_{\mathrm{Fe}})(T_{\mathrm{Fe}}/T)^2$ (Mendell, 1991), where $T_{\mathrm{Fe}} \sim 10^{12}$ is the electron Fermi energy. At $T = 10^7$K, τ of order 10^{-13} s. Hence, we treat muons and electrons as a single component.

4.1.3 Equation of state

The set of equations presented in the last section is closed by an equation of state $\varepsilon(\rho_n, \rho_p, s)$ which relates $\tilde{\mu}_n$, $\tilde{\mu}_p$ and T to the dependent variables. The equation of state has a contribution from neutron and proton degeneracy pressure (Hebeler et al., 2013)

$$\varepsilon_{\text{nuc}} = \frac{\hbar^2}{2m}(3\pi^2)^{2/3}\frac{3}{5}\left[\left(\frac{\rho_n}{m}\right)^{5/3} + \left(\frac{\rho_p}{m}\right)^{5/3}\right], \tag{4.6}$$

and from the degeneracy pressure of the relativistic electron gas:

$$\varepsilon_e = \frac{3\hbar c}{4}(3\pi^2)^{1/3}\left(\frac{\rho_p}{m}\right)^{4/3}. \tag{4.7}$$

Here $\hbar$ is the reduced Planck's constant, c is the speed of light and we take $m_n = m_p = m$. The factor ρ_p/m in Equation (4.7) follows from the assumption of local charge neutrality. Hebeler et al. (2013) parameterize the contribution from strong nuclear interactions as

$$\begin{aligned}\varepsilon_{\text{int}} =& \frac{\hbar^2}{2m}\left(\frac{3\pi^2}{2}\right)^{2/3}\left\{\frac{-1}{{n_0}^{1/3}}\left[(2\alpha - 4\alpha_L)\left(\frac{\rho_n}{m}\right)\left(\frac{\rho_p}{m}\right) + \alpha_L\left(\frac{\rho_n}{m} + \frac{\rho_p}{m}\right)^2\right]\right. \\ &\left. + \frac{1}{n_0^{2/3}}\left(\frac{\rho_n}{m} + \frac{\rho_p}{m}\right)^{1/3}\left[(2\eta - 4\eta_L)\left(\frac{\rho_n}{m}\right)\left(\frac{\rho_p}{m}\right) + \eta_L\left(\frac{\rho_n}{m} + \frac{\rho_p}{m}\right)^2\right]\right\},\end{aligned} \tag{4.8}$$

where $\alpha = 5.87$, $\eta = 3.81$, $\alpha_L = 1.4$, $\eta_L = 0.9$ and $n_0 = 0.16\,\text{fm}^{-3}$ is the nuclear saturation density. Finally, we include thermal effects via the term (Passamonti et al., 2015)

$$\varepsilon_{\text{th}} = \frac{\hbar c(3\pi^2)^{1/3}}{\pi^2 k_B^2}\left(\frac{\rho_p}{m}\right)^{-2/3} s^2. \tag{4.9}$$

Summing the contributions from degeneracy pressure, strong interactions, and thermal effects, we obtain

$$\varepsilon = \varepsilon_{\text{nuc}} + \varepsilon_{\text{e}} + \varepsilon_{\text{int}} + \varepsilon_{\text{th}}. \tag{4.10}$$

The proton and neutron chemical potentials and the temperature are defined by the first law of thermodynamics:

$$d\varepsilon = T\,ds + \tilde{\mu}_n d\rho_n + \tilde{\mu}_p d\rho_p. \tag{4.11}$$

4.1.4 Geometry and boundary conditions

The mass flux (and hence the entropy flux) must vanish at the stellar surface. Because we assume spherical symmetry, the same must be true at the centre. In one-dimension, we impose $v_p = v_n = 0$ at both boundaries, which is consistent with (and enforces) the no-flux condition on the other variables. As initial conditions we take constant densities for ρ_p and ρ_n, and $v_p = v_n = 0$. Similar to the previous chapter, the initial condition for s is a Gaussian near the surface which encodes the initial pulse of heat. The initial densities and temperature (which is a function of ρ_p and s) are of the order of a realistic neutron star: $10^{13}\,\text{g}\,\text{cm}^{-3}$ and $10^8\,\text{K}$ respectively.

We take the neutron star to have radius $R = 10\,\text{km}$, and to again consist of two strata with thermal conductivity given by Equation (3.24). We place the crust-core boundary at $r = 5\,\text{km}$.

In a real neutron star, the boundary is much closer to the surface ($r \approx 1\,\mathrm{km}$). However, in this chapter we are interested in studying the underlying physics, and not creating a realistic model. Placing the boundary at the midpoint of the domain has little impact on the dynamics, while improving the readability of the results.

4.2 Numerical details

Equations (4.1)-(4.4) are first order and hyperbolic, while Equation (4.5) is second order and parabolic. The velocity equations and the entropy equation are nonlinear. Non-linear hyperbolic PDEs are prone to discontinuous solutions (i.e. shock waves), so their numerical implementation must be treated with care.

In one dimension the system of hyperbolic equations (4.1)-(4.4) can be written in the flux-conservative form

$$\frac{\partial u}{\partial t} + \frac{\partial f(u)}{\partial x} = Q. \tag{4.12}$$

Here u, f and Q are vectors of the dependent variables, non-linear fluxes, and right hand side gradient terms, respectively. To solve Equation (4.12) numerically, one can use either first or higher order methods. First order methods have the general advantage of higher stability in the vicinity of a shock wave, but at the cost of numerical accuracy. Higher order methods are more accurate in general, but are prone to exhibiting spurious, high-frequency oscillations near a discontinuity (LeVeque, 1992).

One solution to this trade-off is a flux-limiter scheme, which combines a first order approximation in the vicinity of shock fronts with a higher order method elsewhere in the computational domain. To produce the results in this chapter, I solve Equations (4.1)-(4.4) in one-dimension by implementing the explicit, split-step, Richtmyer Lax-Wendroff algorithm described by Jerez Galiano & Uh Zapata (2010). The algorithm uses conservative upwinding in the predictor step and flux limiting in the corrector step. The entropy equation is solved similarly, but I incorporate an additional split-step in which the diffusion operator is advanced using the implicit Crank-Nicholson algorithm.

4.3 Catalogue of approaches

Over the course of this research, a number of attempts were made to build a consistent model. Before presenting results for the model described in Section 4.1, I discuss some of the lessons learned from these false starts. I initially focused on the Landau two-fluid equations for superfluid ^{4}He; in this section we use the subscripts n (s) for the normal fluid (superfluid). These are, in essence, Equations (4.1)-(4.5), though the pressure terms on the right hand side differ. One challenge was finding an appropriate equation of state, which is needed to specify the chemical potential and temperature. Treating the system as an ideal Bose gas is insufficient here: the chemical potential then vanishes below the transition temperature, which is the regime we are interested in (see Pethick & Smith, 2008, Chapter 2). An explicit equation for the chemical potential is given by Papoular et al. (2012), though it caused the numerical solution to diverge. Surprisingly, taking the negative of that expression produced sensible results. I was not able to explain this. An alternative is to assume the fluids are incompressible: $\nabla \cdot \mathbf{v}_n = 0 = \nabla \cdot \mathbf{v}_s$.

This is a good approximation in a neutron star, where the fluid velocity is much less than the sound speed. Then the pressure terms are fixed implicitly by the incompressibility condition and an equation of state is not needed.

Another, more restrictive assumption is that the net mass transfer vanishes ($\rho_n \mathbf{v}_n = -\rho_s \mathbf{v}_s$). If we also assume that the species ratio ρ_n/ρ_s is approximately independent of temperature, then it is possible to reduce the system to two equations for the temperature and normal fluid velocity:

$$\frac{\partial T}{\partial t} = \frac{\kappa}{\rho c_p}\frac{\partial^2 T}{\partial x^2} - v_n \frac{\partial T}{\partial x} - \frac{s}{c_p}\frac{\partial v_n}{\partial x} + \frac{A(T)\rho^3 \rho_n}{\rho_s^3 c_p} v_n^2 + \frac{A_0}{c_p}\left(\frac{\partial v_n}{\partial x}\right)^2, \tag{4.13}$$

$$\frac{\partial v_n}{\partial t} = A_0 \frac{\rho_s}{\rho_n}\frac{\partial^2 v_n}{\partial x^2} - 3 v_n \frac{\partial v_n}{\partial x} - A(T)\frac{\rho^3}{\rho_s^2} v_n^3 - s\frac{\rho_s}{\rho_n}\frac{\partial T}{\partial x}. \tag{4.14}$$

I initially found this form of the equations appealing, since there existed simple, experimental relations for the dependent variables in terms of the fundamental variables T and v_n. On the other hand, the equations are now second order and less intuitive than in the original, flux-conservative formulation. A further downside is that these equations are unconventional, making it difficult to apply well-known techniques from computational fluid mechanics. I was ultimately unable to write a code which could accurately solve Equations (4.13) and (4.14). A code which treats the pressure terms implicitly is also technically challenging, requiring sophisticated algorithms such as the semi-implicit method for pressure linked equations (SIMPLE), or the pressure-corrected with splitting of operators (PISO) method (see, e.g., Pletcher et al., 2013). Again I was unsuccessful, though in principle I believe this is a sound approach.

After assembling a suitable equation of state, I was able to write and test a code using the finite difference method described in the previous section. In the remainder of this chapter, we study some preliminary results from numerical calculations made with this code.

4.4 Convective and diffusive heating

In this section we consider how the core is heated by the initial surface spike in temperature. The broad astrophysical question is the following: to what extent does the superfluid affect the thermal evolution of the system? To answer this, we would like to gain some sense for the relative importance of diffusive versus non-diffusive heating in different parts of the parameter space.

Figure 4.1 shows, from left to right, the spatially averaged v_p in the core $\langle v_{\mathrm{p}}^{\mathrm{core}} \rangle$ (i.e. the spatial average over the region $r \leq 5\,\mathrm{km}$; flow towards the centre is taken to be positive), thermal energy in the core U_{core}, and central temperature as functions of K and κ_1/κ_2. The broad trend is that higher velocities in the core correlate with larger U_{core}. Consider firstly varying κ_1/κ_2 (in this chapter we focus on the astrophysically relevant regime where $\kappa_1/\kappa_2 \geq 1$). As κ_1/κ_2 increases, U_{core} and $\langle v_p^{\mathrm{core}} \rangle$ decrease. To understand this physically, we plot snapshots of $T(r)$ for various κ_1/κ_2 and weak coupling (Figure 4.2, top left panel). Higher diffusion has the effect of smoothing out the temperature profile, increasing $T(r = 0)$, but reducing the magnitude of the convective term $[\partial(s v_p)/\partial x]$ in the energy equation. There is therefore a competition between the two modes of heating: very strong diffusion tends to quench the convective term. The trade-off is such that the total thermal energy in the core decreases with

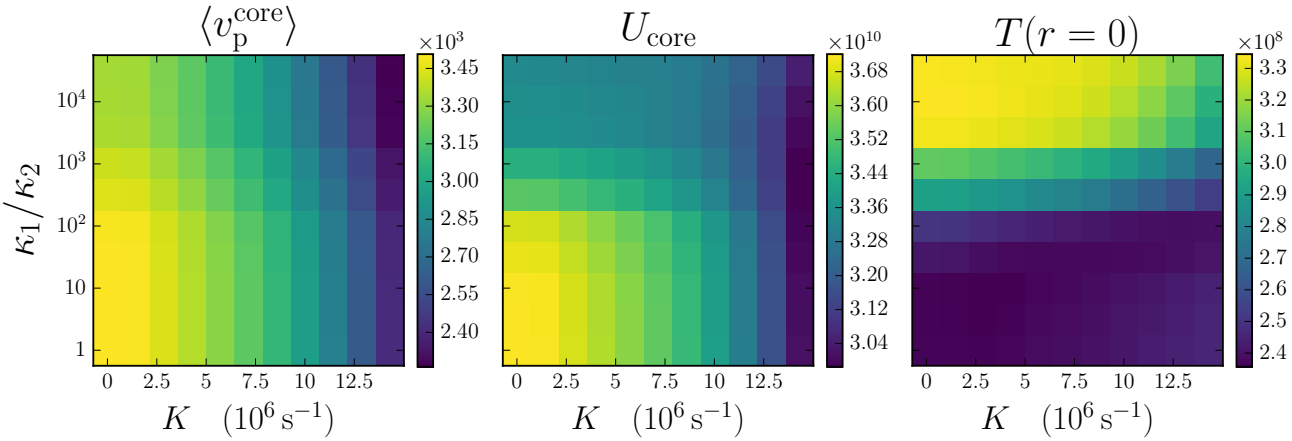

Figure 4.1: Effect of the heat pulse on the core. Left to right: v_p in $\mathrm{m\,s^{-1}}$ spatially averaged over the region $r < 5\,\mathrm{km}$, the thermal energy in the core $U_{\rm core}$, in $\mathrm{J}/(m_{\rm core}c_p)$, and central temperature $T(r=0)$ in K, as functions of κ_1/κ_2 and K, at $t = 2\,\mathrm{s}$.

increasing κ_1/κ_2 ($U_{\rm core}$ decreases in the vertical direction in Figure 4.1). This suggests that convection is important in the regime of small κ_1/κ_2.

We now consider the effect of the coupling coefficient. In Figure 4.1, $\langle v_{\rm p}^{\rm core}\rangle$ decreases with K. This is because the coupling acts to reduce $|v_p - v_n|$ (Figure 4.2, bottom right panel). Recall that the proton-electron fluid carries the entropy. Hence for small v_p the heat is convected more slowly, and $U_{\rm core}$ is also smaller: by $t = 2\,\mathrm{s}$, a smaller fraction of the initial heat pulse has been convected into the core (Figure 4.2, bottom left panel). We find therefore that $U_{\rm core}$, because it depends on v_p, decreases with K (Figure 4.1, middle panel). Finally, consider the central temperature $T(r=0)$ (Figure 4.1, right panel). No part of the temperature wave reaches $r = 0$ by $t = 2\,\mathrm{s}$, so the $T(r=0)$ depends very weakly on K. Diffusion, on the other hand, affects all parts of the domain instantaneously (the heat equation does not obey special relativity), so that $T(r=0)$ increases with κ_1/κ_2.

4.5 Velocity lag at the crust-core boundary

In this section, we comment on a feature of the yellow velocity curve in Figure 4.2 (top right panel): a thin layer at the base of the crust where v_p is large. Figure 4.3 shows that the velocity lag $v_{pn} = v_p - v_n$ also has a local maximum at the base of the crust, which implies that only the proton-electron fluid (and not the superfluid) undergoes a large acceleration here. We expect this from the equations of motion: only s and hence $T(s, \rho_p)$ are sensitive to the conductivities, and the governing equation for v_p depends explicitly on s and T, whereas the equation for v_n does not. Referring again to Figure 4.3, the magnitude of v_{pn} is strongly dependent on the conductivity mismatch between the crust and the core, with larger mismatch giving rise to larger v_{pn}. On the other hand if the core conductivity is very low ($\kappa_1/\kappa_2 < 1$), there is no spike in v_{pn} in this layer.

Relative to the characteristic size of v_{pn}, the lag at the base of the crust appears to depend on the coupling: in Figure 4.3, the scaled size of the peak differs between the left and right panels. To study the dependence on K, we quantify the lag relative to the characteristic flow speed by the ratio of the red and blue curves in Figure 4.3, taken at the local maximum (of the red curve) near $r = 5$: $\eta(K) = v_{pn}^{\rm max}(K, \kappa_1/\kappa_2 = 400)/v_{pn}^{\rm max}(K, \kappa_1/\kappa_2 = 1)$. Table 4.1 shows η for a

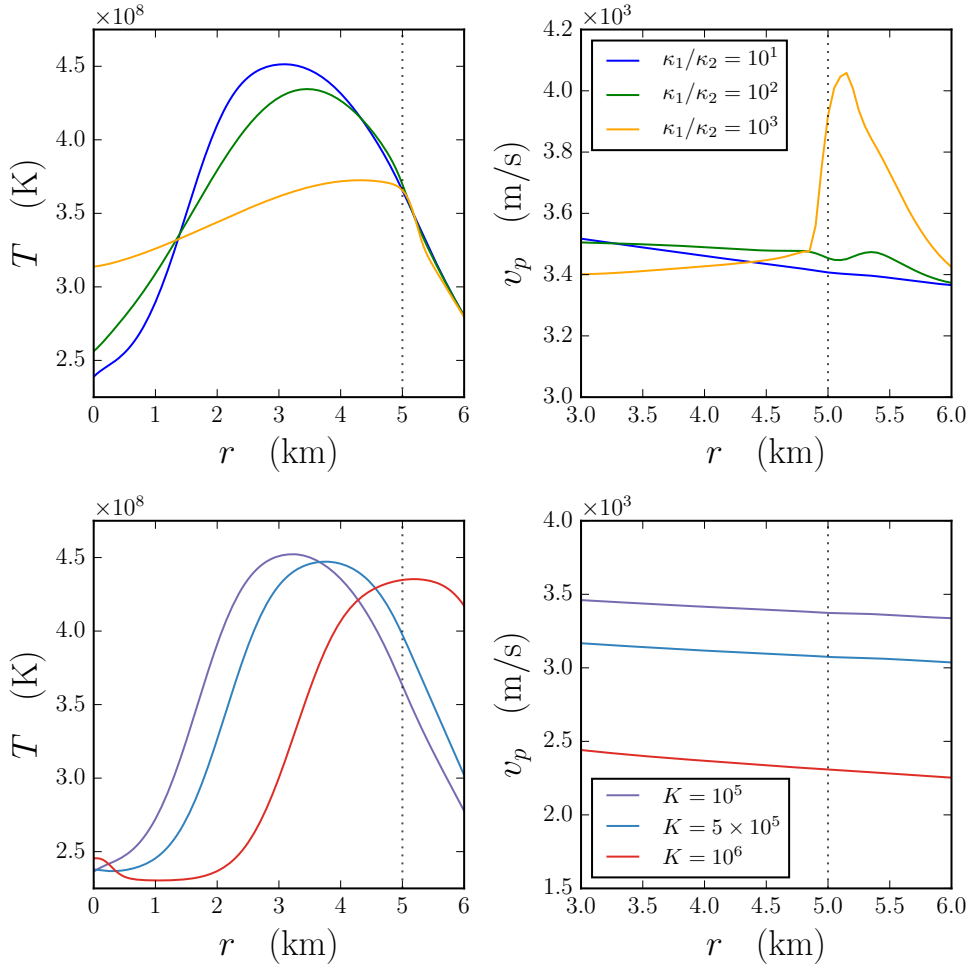

Figure 4.2: Snapshots of the temperature (first column) and velocity (second column) versus r, as functions of κ_1/κ_2 (first row; $K = 10^5\,\mathrm{s}^{-1}$) and K (second row; $\kappa_1/\kappa_2 = 1$), at $t = 2\,\mathrm{s}$.

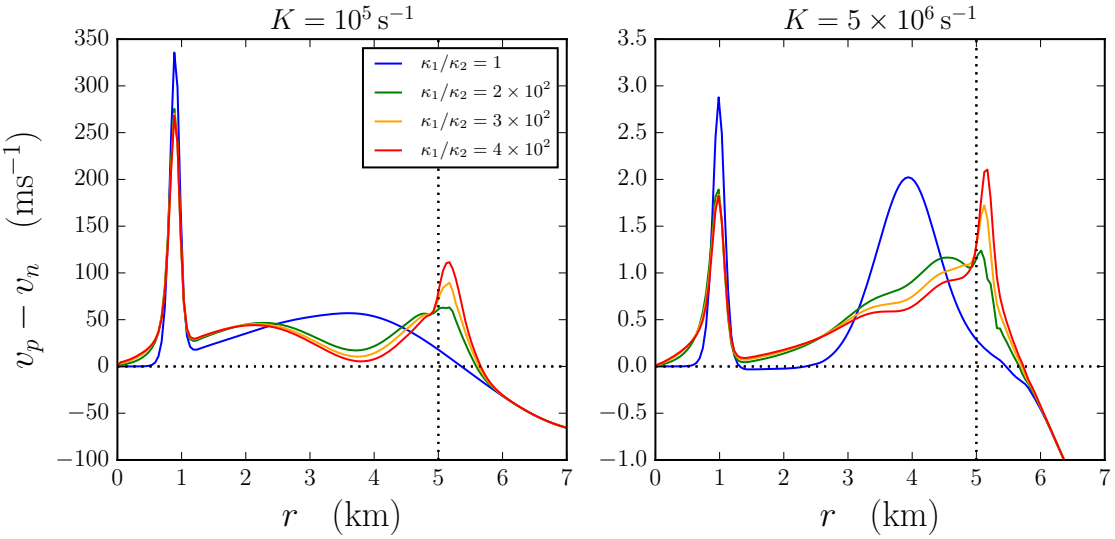

Figure 4.3: Velocity lag $v_p - v_n$ for weak (left) and strong (right) coupling, at $t = 2\,\mathrm{s}$. The conductivity mismatch causes a peak in the crust near $r = 5$. The peak near $r = 1$ corresponds to propagation of the original heating wave. The dotted vertical lines show the location of the crust-core interface. The dotted horizontal lines indicate $v_p - v_n = 0$.

Table 4.1: The relative size of the lag, η (defined in text), for different K.

$K\ (\mathrm{s}^{-1})$	10^5	5×10^5	10^6	5×10^6	10^7
η	17.3	6.7	7.8	14.9	3.8

range of K. We find that η varies in a complicated way with K, though a visual inspection of the graphs confirms that the peak is present for all K studied.

4.6 Conclusions

In this chapter we study how convective heating associated with the superfluid in an accreting neutron star affects the transport of thermal energy into the interior. The model includes coupling between the fluid elements, thermal diffusion, and a finite-temperature equation of state. We describe (Section 4.2) a stable numerical scheme for implementing the model. Some preliminary results are presented. We find (Section 4.4) that high thermal conductivity tends to reduce the impact of the convective term in the energy equation, while convection dominates when the conductivity is low. More energy is deposited in the core when the conductivity is low. This implies, contrary to the conventional view, that convective heating may be important in some situations. In Section 4.5 we show that a conductivity mismatch between strata in a neutron star results in the proton-electron fluid attaining high flow velocities in a layer near the boundary. This layer is present in all cases examined, though the coupling affects the size of the velocities in a complicated fashion. Future work will focus on studying the formation of this layer and clarifying its physical cause.

Chapter 5

Conclusions and future work

This thesis explores two problems relating to the interior of neutron stars: the collective dynamics of superfluid vortices, and the transport of thermal energy in accreting binaries. We briefly summarise the main results below.

- In Chapter 2 we study the collective motion of superfluid vortices in the presence of an annular pinning barrier by solving the time-dependent GPE. The goal is to simulate stratified pinning in the neutron star crust. We find that vortices leave the system at the same rate with and without a moat, but that they tend to accumulate in the moat as the system evolves. We find power-law indices for the distribution of glitch sizes of $\alpha = -0.02$ and -0.81, and mean glitch waiting rates of $\lambda = 0.47$ and 1.44, with and without a moat respectively. We therefore conclude that glitches are larger and less frequent in the presence of a moat.

- Chapter 3 studies diffusive conduction following a deposition of heat in the neutron star crust. We investigate heat transport where the thermal conductivity differs between an inner and an outer region. We find that in the steady state the amount of energy deposited in the core decreases with the core conductivity, given certain boundary conditions. We show that steep temperature gradients can form as heat 'piles up' at the interface between the regions.

- In Chapter 4 we extend these results by solving the hydrodynamic equations for a superfluid neutron star. The goal is to investigate how thermal transport is affected by non-diffusive conduction associated with the superfluid. We find that strong diffusion can limit convective transport. We show that a large conductivity mismatch between the crust and core creates a layer in which the proton-electron fluid velocity is significantly higher than that of the superfluid neutrons.

The goal throughout is not to build realistic models which incorporate the full spectrum of rich physics at play in the neutron star interior. Rather, we aim to understand how the problems studied depend on certain key aspects of the physics. As such, the work provides a useful foundation for future studies. In particular, the implications of asymmetric pinning barriers for gravitational wave emission will be studied. The results in Chapter 4 and the effect on the thermal evolution of large fluid velocities in the boundary layer will also be explored further.

References

Aguilera D. N., Cirigliano V., Pons J. A., Reddy S., Sharma R., 2009, Physical Review Letters, 102, 1

Alford M. G., Schmitt A., Rajagopal K., Schäfer T., 2008, Reviews of Modern Physics, 80, 1455

Allen J. F., Misener A. D., 1938, Nature, 141

Alpar M. A., 1977, The Astrophysical Journal, 213, 527

Alpar M. A., Pines D., Anderson P. W., Shaham J., 1984a, Astrophysical Journal, 276, 325

Alpar M. A., Langer S. A., Sauls J. A., 1984b, Astrophysical Journal, 282, 533

Anderson P. W., Itoh N., 1975, Nature, 256, 25

Andersson N., Comer G. L., 2001, MNRAS, 328, 1129

Andersson N., Comer G. L., 2006, Classical and Quantum Gravity, 23, 5505

Andersson N., Krüger C., Comer G. L., Samuelsson L., 2013, Classical and Quantum Gravity, 30

Avogadro P., Barranco F., Broglia R. A., Vigezzi E., 2007, Physical Review C - Nuclear Physics, 75, 3

Avogadro P., Barranco F., Broglia R. A., Vigezzi E., 2008, Nuclear Physics A, 811, 378

Baert M., Metlushko V. V., Jonckheere R., Moshchalkov V. V., Bruynseraede Y., 1995, Physical Review Letters, 74, 3269

Baym G., Pethick C. J., Pines D., 1969a, Nature, 224, 673

Baym G., Pethick C. J., Pines D., 1969b, Nature, 224, 872

Baym G., Bethe H. A., Pethick C. J., 1971, Nuclear Physics A, 175, 225

Bedaque P. F., Schaefer T., 2002, Nuclear Physics A, 697, 802

Bhattacharya D., 1995, Journal of Astrophysics and Astronomy, 16, 217

Bildsten L., 1998, Astrophysical Journal, 501, L89

Brown E. F., 2000, Astrophysical Journal, 531, 988

Brown E. F., Bildsten L., 1998, Astrophysical Journal, 496, 915

Brown E. F., Cumming A., 2009, Astrophysical Journal, 698, 1020

Brown E. F., Bildsten L., Rutledge R. E., 1998, Astrophysical Journal Letters, 504, L95

Brown E. F., Cumming A., Fattoyev F. J., Horowitz C. J., Page D., Reddy S., 2018, Physical Review Letters, 120, 182701

Chamel N., 2017, Journal of Astrophysics and Astronomy, 38

Chamel N., Haensel P., 2008, Living Rev. Relativity, 11, 10

Chamel N., Naimi S., Khan E., Margueron J., 2007, Physical Review C - Nuclear Physics, 75

Chamel N., Haensel P., Zdunik J. L., Fantina A. F., 2013, International Journal of Modern Physics E, 22

Chamel N., Fantina A. F., Zdunik J. L., Haensel P., 2015, Physical Review C - Nuclear Physics, 91, 1

Chandler E., Baym G., 1986, Journal of Low Temperature Physics, 62, 119

Coleman Miller M., K. Lamb F., 2016, European Physical Journal A, 52

Colpi M., Geppert U., Page D., Possenti A., 2001, The Astrophysical Journal Letters, 548, L175

Comer G. L., Langlois D., Lin L. M., 1999, Physical Review D - Particles, Fields, Gravitation and Cosmology, 60, 1

Cumming A., Brown E. F., Fattoyev F. J., Horowitz C. J., Page D., Reddy S., 2017, Physical Review C, 95, 1

Degenaar N., et al., 2013, Astrophysical Journal, 775

Deibel A., Cumming A., Brown E. F., Reddy S., 2016, Astrophysical Journal, 839, 95

Ding D., Rios A., Dussan H., Dickhoff W. H., Witte S. J., Carbone A., Polls A., 2016, Physical Review C, 94, 1

Donati P., Pizzochero P. M., 2004, Nuclear Physics A, 742, 363

Donati P., Pizzochero P. M., 2006, Physics Letters, Section B: Nuclear, Elementary Particle and High-Energy Physics, 640, 74

Dong J. M., Lombardo U., Zuo W., 2013, Physical Review C, 87, 062801

Drummond L., Melatos A., 2017, MNRAS, 19, 1

Drummond L. V., Melatos A., 2018, MNRAS, 475, 910

Engels P., Coddington I., Haljan P. C., Schweikhard V., Cornell E. A., 2003, Physical Review Letters, 90, 4

Epstein R. I., 1988, Astrophysical Journal, 333, 880

Epstein R. I., Baym G., 1988, Astrophysical Journal, 328, 680

Fetter A. L., 1965, Physical Review, 138, 429

Fuentes J. R., Espinoza C. M., Reisenegger A., Shaw B., Stappers B. W., Lyne A. G., 2017, Astronomy and Astrophysics, 608, 1

Fujimoto M. Y., Hanawa T., Iben I. J., Richardson M. B., 1987, Astrophysical Journal, 315, 198

Gandolfi S., Gezerlis A., Carlson J., 2015, Annual Review of Nuclear and Particle Science, 65, 303

Gardiner C. W., Anglin J. R., Fudge T. I. A., 2002, Journal of Physics B: Atomic, Molecular and Optical Physics, 35, 1555

Gezerlis A., Pethick C. J., Schwenk A., 2014, in Bennemann K.-H., Ketterson J. B., eds, , Novel Superfluids, Volume 2. Oxford University Press, Chapt. 22

Giacconi R., Gursky H., Paolini F. R., 1962, Physical Review Letters, 9, 439

Giacconi R., Gursky H., Kellogg E., Schreier E., Tananbaum H., 1971, Astrophysical Journal

Ginzburg V. L., Kirzhnits D. A., 1965, Journal of Experimental and Theoretical Physics, 20, 1346

Glendenning N. K., 1992, Physical Review D, 46, 1274

Gnedin O. Y., Yakovlev D. G., Potekhin A. Y., 2001, MNRAS, 324, 725

Gualtieri L., Kantor E. M., Gusakov M. E., Chugunov A. I., 2014, Physical Review D - Particles, Fields, Gravitation and Cosmology, 90, 1

Gusakov M. E., Kantor E. M., 2013, Physical Review D - Particles, Fields, Gravitation and Cosmology, 88, 1

Gusakov M. E., Kantor E. M., Haensel P., 2009, Physical Review C - Nuclear Physics, 80, 1

Haensel P., Potekhin A. Y., Yakovlev D. G., 2007, Neutron Stars 1: Equation of State and Structure. Springer-Verlag, New York

Hall H. E., Vinen W. F., 1956, Proceedings of the Royal Society A: Mathematical, Physical and Engineering Sciences, 238, 215

Haskell B., Melatos A., 2015, International Journal of Modern Physics D, 24, 1

Hebeler K., Lattimer J. M., Pethick C. J., Schwenk A., 2013, Astrophysical Journal, 773

Hinkley N., et al., 2013, Science, 341, 1215

Horowitz C. J., Berry D. K., Briggs C. M., Caplan M. E., Cumming A., Schneider A. S., 2015, Physical Review Letters, 114, 1

Itoh N., Kohyama Y., 1994, Astrophysical Journal, 420, 943

Jensen H. J., 1998, Self-Organized Criticality: Emergent Complex Behavior in Physical and Biological Systems. Cambridge University Press

Jerez Galiano S., Uh Zapata M., 2010, Journal of Computational and Applied Mathematics, 234, 1395

Kantor E. M., Gusakov M. E., 2014, MNRAS: Letters, 442, 90

Kapitza P., 1938, Nature, 141

Landau L., 1941, Physical Review, 60, 356

Landau L. D., Lifshitz E. M., 1986, Fluid Mechanics, 2 edn. Vol. 6, Pergamon Press, Oxford

Lattimer J. M., Prakash M., 2004, Science, 304, 536

LeVeque R. J., 1992, Numerical methods for conservation laws. Birkhauser-Verlag, Basel

Lim Y., Hyun C. H., Lee C.-h., 2017, International Journal of Modern Physics E, 26

Linares M., Shahbaz T., Casares J., 2018, Astrophysical Journal, 859, 54

Lindblom L., Mendell G., 1994, Astrophysical Journal, 421, 698

Link B., 2003, Physical Review Letters, 91, 1

Liu Q. Z., van Paradijs J., van den Heuvel E. P. J., 2007, Astronomy and Astrophysics, 469, 807

Lopez-Monsalvo C. S., Andersson N., 2011, Proceedings of the Royal Society A, 467, 738

Melatos A., Peralta C., Wyithe J. S. B., 2008, Astrophysical Journal, 672, 1103

Melatos A., Douglass J. A., Simula T. P., 2015, Astrophysical Journal, 807, 132

Mendell G., 1991, Astrophysical Journal, 380, 515

Migdal A. B., 1959, Zh. Eksp. Teor. Fiz. Pisma, 37, 655

Negele J. W., Vautherin D., 1973, Nuclear Physics, Section A, 207, 298

Ostriker J. P., 1976, in Eggleton P. P., Mitton S., Whelan J., eds, Vol. 73, Proceedings of the IAU Symposium. Springer, Cambridge

Özel F., Psaltis D., Narayan R., Santos Villarreal A., 2012, Astrophysical Journal, 757

Page D., Prakash M., Lattimer J. M., Steiner A. W., 2011, Physical Review Letters, 106, 1

Papoular D. J., Ferrari G., Pitaevskii L. P., Stringari S., 2012, Physical Review Letters, 109, 1

Passamonti A., Andersson N., Ho W. C. G., 2015, MNRAS, 455, 1489

Pethick C. J., Ravenhall D. G., 1995, Annu. Rev. Nucl. Part. Sci., 45, 429

Pethick C. J., Smith H., 2008, Bose-Einstein Condensation in Dilute Gases, 2 edn. Cambridge University Press, New York

Pizzochero P. M., 2011, Astrophysical Journal Letters, 743

Pletcher R. H., Tannehill J. C., Anderson D. A., 2013, Computation Fluid Mechanics and Heat Transfer, 3 edn. CRC Press, Boca Raton

Pons J. A., Viganò D., Rea N., 2013, Nature Physics, 9, 431

Potekhin A. Y., Pons J. A., Page D., 2015, Space Science Reviews, 191, 239

Romani R. W., 1987, Astrophysical Journal, 313, 718

Rutledge R. E., Bildsten L., Brown E. F., Pavlov G. G., Zavlin V. E., Ushomirsky G., 2002, Astrophysical Journal, 580, 413

Schneider B. I., Collins L. A., Hu S. X., 2006, Physical Review E - Statistical, Nonlinear, and Soft Matter Physics, 73, 1

Schreier E., Levinson R., Gursky H., Kellogg E., Tananbaum H., Giacconi R., 1972, Astrophysical Journal, 172

Seveso S., Pizzochero P. M., Grill F., Haskell B., 2016, MNRAS, 455, 3952

Shapiro S. L., Teukolsky S. A., 2004, Black Holes, White Dwarfs, and Neutron Stars: The Physics of Compact Objects. Wiley-VCH, Weinheim

Shin Y., et al., 2004, Physical Review Letters, 93, 6

Shternin P. S., Yakovlev D. G., 2006, Physical Review D - Particles, Fields, Gravitation and Cosmology, 74

Shternin P. S., Yakovlev D. G., Haensel P., Potekhin A. Y., 2007, MNRAS: Letters, 382

Shternin P. S., Yakovlev D. G., Heinke C. O., Ho W. C., Patnaude D. J., 2011, MNRAS: Letters, 412, 1

Simula T. P., Nygaard N., Hu S. X., Collins L. A., Schneider B. I., Mølmer K., 2008, Physical Review A - Atomic, Molecular, and Optical Physics, 77, 4

Tananbaum H., Gursky H., Kellogg E., Levinson R., Schreier E., Giacconi R., 1972, Astrophysical Journal, 143-149

Tauris T. M., van den Heuvel E., 2006, in Lewin W. H. G., van der Klis M., eds, , Compact Stellar X-ray Sources. Cambridge University Press, Cambridge, Chapt. 16

Thorne K. S., 1977, Astrophysical Journal, 212, 825

Tkachenko V. K., 1966, Soviet Physics JETP, 23, 1049

Tung S., Schweikhard V., Cornell E. A., 2006, Physical Review Letters, 97, 2

Ushomirsky G., Rutledge R. E., 2001, MNRAS, 325, 1157

Viganó D., Rea N., Pons J. A., Perna R., Aguilera D. N., Miralles J. A., 2013, MNRAS, 434, 123

Vodicka V., 1950, Schweizer Archiv, 10, 297

Warszawski L., 2011, Phd, The University of Melbourne

Warszawski L., Melatos A., 2011, MNRAS, 415, 1611

Warszawski L., Melatos A., 2012, MNRAS, 423, 2058

Warszawski L., Melatos A., 2013, MNRAS, 428, 1911

Warszawski L., Melatos A., Berloff N. G., 2012, Physical Review B - Condensed Matter and Materials Physics, 85

Wijnands R., Heinke C. O., Pooley D., Edmonds P. D., Lewin W. H. G., Grindlay J. E., Jonker P. G., Miller J. M., 2005, Astrophysical Journal, 618, 883

Wlazłowski G., Sekizawa K., Magierski P., Bulgac A., Forbes M. M. N., 2016, Physical Review Letters, 117, 1

Yakovlev D. G., Kaminker A. D., Gnedin O. Y., Haensel P., 2001, Physical Reports, 354, 1

Yakovlev D. G., Gnedin O. Y., Gusakov M. E., Kaminker A. D., Levenfish K. P., Potekhin A. Y., 2005, Nuclear Physics A, 752

Zeldovich Y. B., Guseynov O. H., 1966, Astrophysical Journal, 144, 840